NKS-443
ISBN 978-87-7893-535-9

Barsebäck as a Research and Development Platform, Extraction and Analysis of Service-aged and Irradiated Reactor Pressure Vessel Material

Pål Efsing[1,4], Magnus Boåsen[1], Daniela Klein[1]

Ulla Ehrnstén[2], Pentii Arffman[2], Noora Hytönen[2]

Jari Lydman[2],Sebastian Lindqvist[2]

Mattias Thuvander[3], Kristina Lindgren[3]

Jenny Roudén[4]

[1] Department of Solid Mechanics, Royal Institute of Technology (KTH), SE-10044 Stockholm Sweden
[2] VTT Technical Research Centre of Finland Ltd, PO Box 1000, FI-02044 VTT, Helsinki, Finland
[3] Chalmers University of Technology, Department of Physics, SE-41296, Göteborg, Sweden
[4] Ringhals AB, SE-43285 Väröbacka, Sweden

February 2021

Abstract

As part of the NKS-R program, VTT, Chalmers University of Technology and KTH has continued the mechanical and microstructural testing in order to analyze the as-aged material properties of the retired reactor pressure vessel, RPV, and reactor pressure vessel head, RPVH from Barsebäck unit 2. The current phase included Impact testing of material from the reactor pressure vessel head and microstructural characterization of the weld metal using LOM, SEM and APT. Due to the nature of the work, the NKS-project is connected to a number of adjacent activities, including support from the Finnish Nuclear Safety Program, the SAFIR-program, the Swedish Radiation Safety Authority SSM and Swedish Centre for Nuclear Technology, SKC and Energiforsk.

Magnus Boåsen, KTH and Sebastian Lindqvist, VTT/Altoo University both successfully presented and defended their Ph.D. theses partially performed with-in the scope of the project during the fall of 2020.

Key words

Low alloy steel, Long Term Operation, irradiation effects, fracture toughness, ductile to brittle transition temperature, constraint effects, high resolution microscopy, microstructural characterization

NKS-443
ISBN 978-87-7893-535-9
Electronic report, February 2021
NKS Secretariat
P.O. Box 49
DK - 4000 Roskilde, Denmark
Phone +45 4677 4041
www.nks.org
e-mail nks@nks.org

Barsebäck as a Research and Development Platform, Extraction and Analysis of Service-aged and Irradiated Reactor Pressure Vessel Material

Final Report from the NKS-R BREDA-RPV 2020 activity

(Contract: AFT/NKS-R(20)118/1)

Pål Efsing[1,4], Magnus Boåsen[1], Daniela Klein[1]
Ulla Ehrnstén[2], Pentti Arffman[2], Noora Hytönen[2], Jari Lydman[2], Sebastian Lindqvist[2]
Mattias Thuvander[3], Kristina Lindgren[3]
Jenny Roudén[4]

[1] Department of Solid Mechanics, Royal Institute of Technology (KTH), SE-100 44 Stockholm Sweden
[2] VTT Technical Research Centre of Finland Ltd, PO Box 1000, FI-02044 VTT, Espoo, Finland
[3] Chalmers University of Technology, Department of Physics, SE-412 96, Göteborg, Sweden
[4] Ringhals AB, SE-43285 Väröbacka, Sweden

Table of contents

1. Introduction

As a part of the NKS-R program in 2020, VTT, Chalmers University of Technology, and KTH have continued the efforts previously outlined in the summary report from 2016, 2018 and 2019 [Efsing et al. 2016, Efsing et al 2018, Efsing et al. 2019]. The project consists of extraction, mechanical and microstructural testing, and analysis, of materials from a retired reactor pressure vessel, RPV, from the now shut-down Barsebäck Nuclear Power Plant. The objective of the study is to increase the current knowledgebase on the correctness of the existing surveillance programs, as well as the influence of long time thermal ageing of materials used for large pressure vessels in the nuclear industry such as the RPV and Pressurizer, PRZ. In the first stage during 2016, a baseline study of the mechanical properties of the used materials was performed- The objective of this was to establish a technical basis for a test program to analyze the “as-aged” material properties of the RPV from Barsebäck unit 2. Further, the program regarding the extraction methodology and the actual materials harvesting was outlined and initial qualification of the methodologies performed. Baseline assessment of the mechanical properties, literature studies and gathering of background information to support the testing of actual harvested materials was also part of the original scope. The harvesting work has been fully financed by Ringhals AB, Forsmark Kraftgrupp AB and OKG AB as part of an umbrella project under the auspices of Energiforsk with Monika Adsten as the primary program manager. The work connects to the BRUTE program, currently in progress under the Finnish nuclear safety research program, SAFIR2022.

In 2018, the actual extraction of the material took place with follow on activities related to obtaining the permission from the Swedish and Finnish radiation protection authorities to allow for shipping of the specimens from Sweden to Finland for mechanical testing. Studies on archive materials, and studies on other material with similar chemistries was also performed. In 2019, the work consequently proceeded with mechanical and microstructural assessment of the thermally aged material harvested from the Reactor Pressure Vessel Head, RPVH, of Barsebäck unit 2.

In 2020, the main progress has been in the area of mechanical testing and microstructural characterization of the materials from the RPVH. Impact tests and hardness measurements have been shown to be confirmative to each other, here supporting suggestions made by Efsing et al [2014] with respect to assessment of the effect of irradiation on the tensile and fracture mechanical properties to utilize hardness as an indicator for future test extension. Further the microstructural characterization of the samples has been extended to include also the beltline weld which has been partially reported.

The key deliverable during BREDA-RPV 2020 was the technical meeting which, due to the pandemic situation, was held as a web-seminar hosted by VTT on the 22nd of September 2020, attracting approximately 50 participants from the academic, industry and regulatory side. At the seminar, all of the young generation researchers were given opportunities to present their work to allow for cross examination and interaction with the research community.

Apart from this, Magnus Boåsen, KTH and Sebastian Lindqvist, VTT both defended their theses with excellence during the fall which brings the number of successful Ph. D. theses to 3 within the network developed through the project. The two most recent theses from the research group active in the project can be found at:

https://www.diva-portal.org/smash/record.jsf?pid=diva2%3A1457162&dswid=-5189

https://aaltodoc.aalto.fi/handle/123456789/46386

Note that Sebastian's work primarily was performed on Nickel based weld metal albeit his work is central to the fracture mechanical testing performed at VTT.
The thesis by Boåsen [Boåsen 2020] contains a framework for modelling of the behavior of aged low alloy steel that can be utilized for the future work as envisaged in the proposal for the coming years for BREDA.

The mechanical testing work at VTT has been complimented by a separate study of how to reliably produce an initial defect for mechanical testing of samples with shallow edge defects at KTH, which is being implemented in other testing projects, and nanostructure studies of the material from Barsebäck at Chalmers. The sum of these efforts lays a firm foundation for future work with the irradiated and thermally aged material.

In February 2020, Kristina Lindgren, Chalmers, and Magnus Boåsen, KTH, visited VTT in Espoo to interact with the research team there and to perform annealing and hardness measurements of Ringhals surveillance and materials test reactor irradiated RPV weld metal, to match the atom probe tomography, APT, analysis of the same materials earlier annealed at Chalmers. Since the exact annealing temperature was found to be crucial at these temperatures, the same material will be sent to Chalmers for complementary APT analysis early 2021.

2. Preliminary mechanical test matrix for the BREDA/BRUTE project

A report describing the proposed work scope for the testing of mechanical properties of the material harvested from Barsebäck unit 2 was developed in a draft version during 2018 and finalized in 2019. [Boåsen 2019]. The report was transmitted to NKS as part of the reporting 2018 [Efsing et al. 2019]. According to the proposal, it was suggested that the test matrix includes testing of miniature Compact Tension, C(T), and Single Edge Notch Bend, SE(B) specimens to evaluate ductile and cleavage fracture behaviour and the influence of constraint on the mechanical properties. In addition to this, the proposed testing will include Charpy-V impact test specimens, microstructural samples, hardness measurements and tensile test specimens to fully categorize the mechanical properties of the aged material.

The test matrix has since then been finalized by VTT and will be described in the BRUTE Summary report for 2020 [Ehrnstén 2020]. The report also describes the verification work performed to qualify the new hot-cell laboratory of VTT for work in the area.

3. Mechanical properties of thermally aged RPV steel from Barsebäck unit 2

VTT has determined the transition curve for the reactor pressure vessel head weld metal by performing impact tests on 23 specimens removed from the 1/4T depth from the inner surface of the two of the delivered trepans from the RPVH. Analyses of the test results included impact energy and crack arrest force transition curve determinations as well as correlation evaluation between impact energy and lateral expansion and shear fracture appearance. When compared to the baseline results, the results indicate that the shift in the transition temperature for the weld metal is insignificant due to thermal embrittlement (280°C for 28 years). The brittle to ductile transition temperature (DBTT) T_{41J} was -75°C, and equal to that of the unirradiated and unaged baseline data. The results thus show that 28 years of operation has not changed the DBTT due to thermal ageing. The tensile properties of the SAW weld metal from the RPVH have been determined at four different temperatures, i.e., room temperature, 125 °C, 288 °C and 300 °C and results are similar to those of the baseline results. The results from the impact toughness tests of the weld metal were confirmed in Q4/2020 from fracture toughness testing using miniature C(T) specimens. These were cut from the tested impact toughness test specimens and revealed similar T0 values for the RPVH weld to that of the base line weld.

KTH performed work on a weakest link model for brittle fracture that uses state of the art Finite Element Modeling (FEM) to study the effect of constraint on thermally aged material. The main bulk of the work is reported in [Boåsen 2020]. The framework is also used in the expansion work that is performed by Daniela Klein at KTH. This will be reported in future reports on the progress of the project. Additionally, Shuyue Wang has started a complimentary project at KTH, supported by SKC, Swedish Centre for Nuclear Technology, aiming at expanding the modelling framework into the ductile failure regime. Thus, two further students will be included in the future work and networking.

4. Microstructural analysis of weld metal

Noora Hytönen has in 2020 accepted a position at VTT as student researcher with the objective to pursue a Ph.D. thesis in addition to performing the microstructural work connected to the BRUTE project.

So far, detailed fractographic and microstructural investigations were performed on the impact and toughness specimens from the RPVH weld metal, see for example [Hytönen et al 2019]. Initiation at secondary particles was observed with lower roughness values correlating to larger initiating particles. Both broken and debonded particles were observed. The investigations revealed also an effect of the microstructure on the toughness, being lower when initiation occurs in the re-heated microstructure compared to as-welded microstructure. A scientific paper on the results from the impact toughness specimen´s investigation is in press [Hytönen 2020, submitted to International Journal of Minerals, Metallurgy and Materials for publication].

The microstructures of the beltline materials are similar to those of the RPVH weld metal. The hardness is slightly lower than that of the RPVH materials, as are the weld tensile properties.

5. Microstructural assessment of aged material using Atom Probe Tomography (APT)

At Chalmers, the nanometre scale chemistry within the beltline weld metal has been studied using APT in addition to the other materials included in Kristina Lindgren’s work. The material from Barsebäck was exposed to 7.9 10^{21} n/m^3 in a weld during the lifetime of B2. As expected in a BWR, no well-defined nanometre sized clusters containing Ni, Mn, Si, and Cu, have been identified, as seen in Figure 1.

Early 2020 complementary APT runs were done by Kristina to the Barsebäck RPV beltline weld metal, in a straight flight path atom probe at Oxford University. The hope was that the newer instrument with higher detection efficiency could improve the statistics in order to better understand the small fluctuations from random in the position of the Ni atoms within the material.

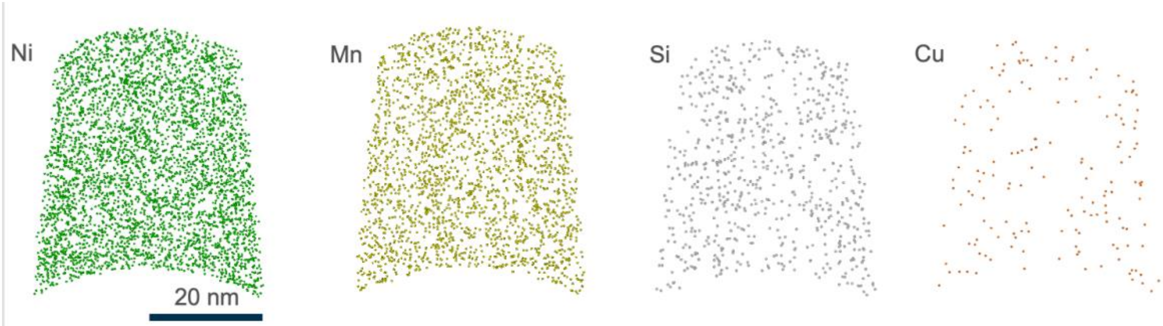

Figure 1. 5 nm thick slices from the APT reconstruction of the analysis of the irradiated material. No clusters are observed.

This idea stemmed from the previous observation that there might be some statistical tendencies of clustering of Ni atoms. When comparing the Ni-Ni radial distribution function (RDF) of the irradiated material with that of the reference material that was also analysed using APT, there is a larger tendency of Ni atoms to be close to other Ni atoms after neutron irradiation. However, it was found that the decreased mass-resolution of the instrument made these attempts futile. During the week that she was visiting, Kristina also gave a seminar on her work to the Oxford APT group.

Here it can also be noted that Kristina was awarded the Sigvard Eklund's Prize for best PhD thesis for 2020 at the annual SKC seminar in October 2020.

6. Conclusions

Samples have been extracted from the RPV of Barsebäck Unit 2 and those from the RPV head included in this program has been transported to VTT. Several milestones of the project were completed in 2020, i.e. the test lab was qualified for tests on active material, the mechanical testing of the RPVH was for most finalized, and work on the irradiated material from the belt line commenced.

The current state of the art regarding the influence of constraint on fracture properties have been summarized and reviewed with the objective to lay a firm foundation for the envisaged testing. A finite element analysis has been performed to support the forth coming mechanical testing using fracture mechanical test techniques.

An international open workshop has been held to promote the project and to report the work externally in September of 2020. Sebastian Lindqvist and Magnus Boåsen both defended their respective theses during the fall of 2020. Both disseminations were held as virtual meetings.

7. References

Arffman P., Impact test results from B2 RPV head SAW weld metal, VTT Research Report VTT-R-00942-19, 2019, 47 pages.

Boåsen M. et al, Preliminary mechanical test matrix for the BREDA-BRUTE project, VTT Research Report VTT-R-06849-18, 2019, 24 pages

Boåsen M., Modeling of structural integrity of aged low alloy steels using non-local mechanics, Ph.D. Thesis, KTH, 2020, 55 pages, ISBN: 978-91-7873-603-4 (digital)

Efsing P et al. 2016, Barsebäck as research and development platform, extraction and analysis of reactor pressure vessel material, Final report for the BREDA2016 activity, NKS-385, ISBN 978-87-7893-471-0.

Efsing P et al., 2018 Barsebäck as research and development platform, extraction and analysis of reactor pressure vessel material, Final report for the BREDA2018 activity, NKS-418, ISBN 978-87-7893-507-6.

Efsing P et al, 2019 Barsebäck as research and development platform, extraction and analysis of reactor pressure vessel material, Final report for the BREDA2018 activity, rev 1, NKS-431, ISBN 978-87-7893-521-2.

Efsing P et al, 2014 Flux Effects on Radiation Induced Aging Behaviour of Low Alloy Steel Weld Material with High Nickel and Manganese Content, In ASTM-STP 1572, Effects of Radiation on Nuclear Material, ASTM, West Conshohocken, PA, USA, doi: 10.1520/STP157220130112.

Ehrnstén U. et. al., 2020 Barsebäck reactor pressure vessel material used for true evaluation of embrittlement (BRUTE), SAFIR yearly report, to be published.

Hytönen N. 2019 Effect of microstructure on brittle fracture inititation in a reactor pressure vessel weld material, Masters Thesis, November 2019, Tampere University.

Hytönen N. et al., 2020 Effect of weld microstructure on brittle fracture initiation in a thermally aged boiling water reactor pressure vessel head weld metal, To be published in International Journal of Minerals, Metallurgy and Materials.

Acknowledgements

NKS conveys its gratitude to all organizations and persons who by means of financial support or contributions in kind have made the work presented in this report possible.

The support from the Finnish nuclear safety program, the SAFIR2022-program, the Swedish Radiation Safety Authority and the Swedish Centre for Nuclear Technology, SKC and finally the Swedish Nuclear Power Plants permit holders and owners (Ringhals AB, Forsmarks Kraftgrupp AB, OKG AB, Vattenfall AB and Uniper) for the work is gratefully acknowledged. Some of the adjacent work is part of a research program coordinated by Energiforsk with Monika Adsten as the program manager

Appendices

1. Boåsen et al., “Analysis of thermal embrittlement of a low alloy steel weldment using fracture toughness and microstructural investigations”, Manuscript pending submission to journal, 35 pages

2. N Hytönen et al., “Effect of weld microstructure on brittle fracture initiation in a thermally aged boiling water reactor pressure vessel head weld metal”, To be published in International Journal of Minerals, Metallurgy and Materials, In press. 12 pages

Title	Barsebäck as a Research and Development Platform, Extraction and Analysis of Service-aged and Irradiated Reactor Pressure Vessel Material
Author(s)	Pål Efsing[1,4], Magnus Boåsen[1], Daniela Klein[1] Ulla Ehrnstén[2], Pentii Arffman[2], Noora Hytönen[2], Jari Lydman[2], Sebastian Lindqvist[2] Mattias Thuvander[3], Kristina Lindgren[3] Jenny Roudén[4]
Affiliation(s)	[1] Department of Solid Mechanics, Royal Institute of Technology (KTH), SE-10044 Stockholm Sweden [2] VTT Technical Research Centre of Finland Ltd, PO Box 1000, FI-02044 VTT, Helsinki, Finland [3] Chalmers University of Technology, Department of Physics, SE-41296, Göteborg, Sweden [4] Ringhals AB, SE-43285 Väröbacka, Sweden
ISBN	978-87-7893-535-9
Date	February 2021
Project	NKS-R / BREDA2020 activity (Contract: AFT/NKS-R(20)118/1)
No. of pages	7
No. of tables	0
No. of illustrations	1
No. of references	9

Abstract
max. 2000 characters

As part of the NKS-R program, VTT, Chalmers University of Technology and KTH has continued the mechanical and microstructural testing in order to analyze the as-aged material properties of the retired reactor pressure vessel, RPV, and reactor pressure vessel head, RPVH from Barsebäck unit 2. The current phase included Impact testing of material from the reactor pressure vessel head and microstructural characterization of the weld metal using LOM, SEM and APT. Due to the nature of the work, the NKS-project is connected to a number of adjacent activities, including support from the Finnish Nuclear Safety Program, the SAFIR-program, the Swedish Radiation Safety Authority SSM and Swedish Centre for Nuclear Technology, SKC and Energiforsk.

Magnus Boåsen, KTH and Sebastian Lindqvist, VTT/Altoo University both successfully presented and defended their Ph.D. theses partially performed with-in the scope of the project during the fall of 2020.

Key words Low alloy steel, Long Term Operation, irradiation effects, fracture toughness, ductile to brittle transition temperature, constraint effects, high resolution microscopy, microstructural characterization

Analysis of thermal embrittlement of a low alloy steel weldment using fracture toughness and microstructural investigations

Magnus Boåsen[a] *, Kristina Lindgren[b], Martin Öberg[a],
Mattias Thuvander[b], Jonas Faleskog[a], Pål Efsing[a]

[a] *Solid Mechanics, Department of Engineering Mechanics, KTH Royal Institute of Technology, SE-100 44 Stockholm Sweden*

[b] *Department of Physics, Chalmers University of Technology, SE-412 96 Göteborg, Sweden*

Abstract

A thermally aged low alloy steel is investigated in terms of its fracture toughness and microstructural evolution and compared to a reference. The main purpose of the study is to investigate the effects of thermal embrittlement on the brittle fracture toughness, and its effects on the influence of loss of crack tip constraint. Ageing appears to enable brittle fracture initiation from grain boundaries besides initiation from second phase particles, making the fracture toughness distribution bimodal as a result. The effect is that the constraint effect is significantly reduced when grain boundary initiation dominates the toughness distribution, as compared to the reference material where the constraint effect is significant. The microstructure is investigated at the nano scale using atom probe tomography where nanometer sized Cu-rich clusters are found primarily situated on dislocation lines.

---

* Corresponding author.
Address: KTH Solid Mechanics, Teknikringen 8D, SE-100 44 Stockholm Sweden
Email address: boasen@kth.se (M. Boåsen)

1. Introduction

When assessing degradation due to ageing in low alloy steels used as structural materials in pressure vessel components both base and weld metals must be considered, as for example in reactor pressure vessels in nuclear power plants. In this type of materials in nuclear applications, ageing mainly occurs by neutron irradiation and thermal ageing, and generally manifest itself as a hardening effect and an increase in the ductile-to-brittle transition temperature, or in another word *embrittlement*. In pressurized water reactors (PWR), the pressurizer regulates the pressure and thereby the temperature within the primary loop so that the water is kept from boiling. Following the replacement of the pressurizer in Ringhals unit 4 (R4) in 2011, material extraction was carried out in order to study potential ageing effects on the materials after 28 years of operation. Initial investigations of two of the welds from the pressurizer material displayed a noteworthy increase in the transition temperature ΔT_{41J} = {78 and 71} ˚C and an increase of the yield strength ΔR_{p02} = {128 and 59} MPa, displaying a clear indication of embrittlement due to thermal ageing at the operating temperature of 345 ˚C (no irradiation present in the pressurizer).

Embrittlement is a key aspect in the structural integrity ageing assessment of any structure. Therefore, understanding the changes in the fracture toughness and all its features for a material that undergoes embrittlement is necessary. The cleavage fracture toughness of ferritic steels is strongly dependent on temperature, size and crack tip constraint. Generally, it can be said that higher temperature endorses a more ductile behavior, larger specimens or components will be more brittle, and high constraint will produce a lower fracture toughness than low constraint. To our knowledge, no studies has been published concerning the constraint effect on fracture toughness after the material has undergone embrittlement and how this relates to the behavior of a reference material.

The prevailing explanation to embrittlement due to thermal ageing of low alloy steels in nuclear applications is impurity segregation towards prior austenite grain boundaries, e.g. phosphorus, commonly referred to as grain boundary embrittlement. Studies of thermal ageing include a wide spectra of base and weld metals from reactor types such as the VVER-1000 [1], [2], [3], [4], as well as the western PWRs featuring the typical steels A508 and A533 or its equivalents [5], [6], [7], [8], [9], [10], [11]. All studies referenced here, reports on intergranular fracture due to impurity segregation caused by thermal ageing.

In the extensive review of intergranular failure in steels by Briant and Banerji [12], it is noted that some distinguishable phenomena appear to be related to intergranular failure. One being that segregation of elements from groups IV-VI in the periodic system appears to yield the most potent grain boundary embrittlement, which is also mentioned by McMahon [13]. These groups include elements such as Si, Sn, P and S, which are not uncommon impurities or alloying elements in the steels of interest. Another is that a grain size effect appears to emerge where larger grains yields more intergranular fracture, the authors of [12] speculate that this could be due to a dilution of the impurity elements due to differences in grain boundary area in relation to grain volume. This implies that a microstructure with smaller grains would result in a larger degree of dilution of impurity across the grain boundaries and thus less embrittlement, than in a microstructure with larger grains *ceteris paribus*. Another notable phenomenon is the effect of co-segregation of elements such as Ni and Mn, which is indicated to yield a faster and more potent embrittlement [12], [14], [15]. In a study by Banerji et al. [16] concerning the effects of impurities and hydrogen on intergranular fracture in a commercial steel, several heats were tempered at different temperatures in the range 50-625 ˚C and then subjected to Charpy impact testing at room temperature. One of the findings in the study was that the largest decrease of the absorbed energy appeared after tempering at ~350 ˚C with resulting intergranular facets covering the fracture surfaces. Also, a similar grain size dependency as reported in [12] could be observed, i.e. larger grains yielding more embrittlement at the same conditions.

Grain boundary embrittlement as a result of thermal ageing will act as a non-hardening embrittlement since it, in general, does not impede dislocation motion, and gives rise to a fracture morphology with a large incidence of grain boundary facets. It also appears to have several commonalities with the phenomenon called reversible temper embrittlement [12], [17]. The hardening effect that is typically observed in irradiated low alloy steels comes to a large extent from the formation of solute clusters during irradiation. The hardening effect is due to that the solute clusters acts as obstacles to dislocation motion, thereby increasing the resistance to plastic flow. In the case of the welds of the Swedish reactor pressure vessels, the irradiation induced solute clusters consists mainly of Mn, Ni, Si and Cu [18], [19], [20]. The formation of similar clusters in a thermally aged weld metal has also been observed by Lindgren et al. [21]. In that study, solute clusters are noted to have been formed preferentially on dislocations as observed by atom probe tomography (APT) and is related to the thermally ageing induced hardening of the weld metal. It should be noted that the weld investigated in this study and the one investigated by Lindgren et al. were extracted from the same pressurizer but from different welds. However, both welds were manufactured with the same welding specifications. In other atom probe studies of thermally aged low alloy steels [22], [23], [24], [25], solute clusters of similar composition of the ones in [21] were found, however these findings were not connected to any changes in mechanical properties.

The weld investigated in this study is a multi-layer weld, which signifies that the weld is built up by several layers of weld beads. This gives rise to a complex microstructure where three distinct grain zones will emerge. These zones are:

I. the as welded zone, consisting of elongated dendritic grains,

II. the once reheated zone, consisting of small eqiaxed grains, and

III. the multiple reheated zones, also consisting of small equiaxed grains.

This will give rise to variations in several properties such as local chemistry, fracture toughness and other mechanical properties. An interesting study of the fracture toughness of multi-layer welds was made by Viehrig et al. [26].

The main purpose with the testing conducted in this paper is to investigate the effects of thermal ageing on the cleavage fracture toughness, and its effects on the influence of loss of constraint. Due to the fact that ageing also may lead to weakened grain boundaries, it is also of interest to investigate to what extent this may contribute to the embrittlement, where weakened grain boundaries then will introduce a second mechanism for brittle fracture initiation besides initiation from particle cracking. Thus, the core of this paper is an investigation of the fracture toughness of an in-service thermally aged weld metal from a Swedish nuclear power plant. This is compared to a reference material from a replaced reactor pressure vessel head, which has been in operation at a lower temperature than the pressurizer and where the effects of ageing therefore are considered minor. The study presents the results from an extensive experimental program where effects of ageing on the constraint sensitivity has been a focal point. Moreover, results from ductile fracture toughness testing, and tensile as well as hardness testing are presented along with an examination of the materials microstructure on the nano scale.

The outline of the paper is as follows: Section 2 presents the materials used in this study in terms of chemical composition, as manufactured mechanical properties, along with the experimental set-up used. Section 3 presents the outcome of the experimental program including fractography and results from and atom probe tomography.

2. Materials and experiments

2.1. Materials

The thermally aged material investigated in this study has been extracted from the decommissioned and replaced pressurizer of the Ringhals unit 4 reactor. The pressurizer was manufactured by Uddcomb from plates of low alloy steel of the type A-533 Gr B Cl. The investigated weld metal in this study comes from the circumferential weld connecting the lower head to the first cylindrical structure of plates in the pressurizer. The studied weld was manufactured using submerged-arc welding employing a weld wire with a low Cu – high Mn-Ni content, characteristic for several of the nuclear pressure vessels manufactured by Uddcomb. The measured chemical composition of the weld wire and flux combination can be found in Table 1. A post weld heat treatment was conducted for residual stress relief at 620 ˚C as part of the fabrication procedure. The pressurizer was in operation between 1983 to 2011, gathering 215 000 h at an operating temperature of 345 ˚C. The pressurizer was well insulated during its operation and consequently the temperature gradient through the thickness can be considered negligible. The check-in mechanical testing of the weld metal can be found in Table 2. The material from the pressurizer will henceforth be denoted as *R4PRZ*.

A reference material extracted from the replaced reactor pressure vessel head of Ringhals unit 3, was also included in the testing program for comparison purposes. This material was chosen since there was no archive material available for the pressurizer. A weld with similar Cu-Mn-Ni-Si content and check-in mechanical properties as the pressurizer was chosen. The reactor pressure vessel head was manufactured from forgings of A-508 cl 2 by Uddcomb and was welded using the same manufacturing specifications as the pressurizer of Ringhals unit 4. The measured chemical composition of the reference material can be found in Table 1, and the check-in mechanical properties in Table 2. The reference material was in operation between 1981 and 2005 accumulating 176 000 h at 310-315 ˚C. Preliminary testing (not presented here) showed that the effects of thermal ageing at this operating temperature were minor in comparison to those of the pressurizer. The reference material will be denoted as *R3RPVH* throughout this paper.

Table 1 Chemical composition of the investigated weld metals from the manufacturing documentation.

Wt. %	C	Si	P	S	V	Cr	Mn	Co	Ni	Cu	Mo	Sn	Fe
R4PRZ	0.082	0.20	0.013	0.006	0.004	0.14	1.62	0.008	1.61	0.06	0.45	0.005	Bal.
R3RPVH	0.08	0.22	0.008	0.006	0.000	0.03	1.66	0.019	1.57	0.07	0.49	0.002	Bal.

Table 2 Check-in mechanical properties of the investigated weld metals.

	R_{p02}/MPa	T_{41J}/°C
R4PRZ	579	-53
R3RPVH	575	-59

2.2. Fracture testing

The fracture toughness testing in the investigation of the constraint effect utilizes SEN(B)-specimens with the same overall dimensions but with different crack depth, deep for a state of high constraint and shallow for low constraint, for an illustration see Figure 1. Also included in the study is a small, deeply cracked SEN(B)-specimen as a reference specimen. All specimens were extracted as T-S oriented with dimensions W = {30 and 14} mm, B = {15 and 7} mm, a/W = {0.5 and 0.1}, and were manufactured such that the weld was centered in the specimen with base metal on each side. All specimens for investigation of the cleavage fracture toughness were manufactured without side grooves.

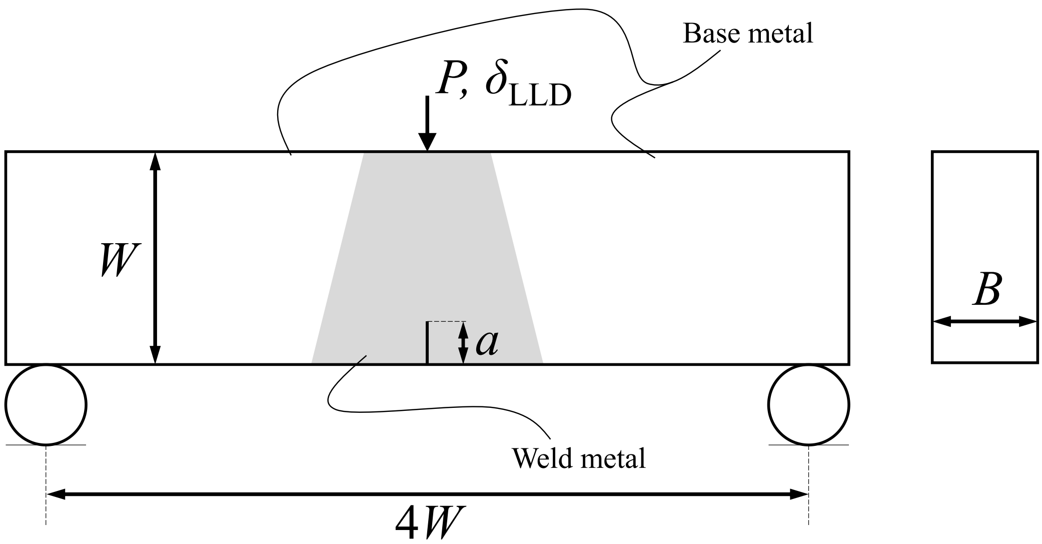

Figure 1. Schematic illustration of a SEN(B)-specimen used in the experiments.

The testing for the cleavage fracture toughness was conducted in accordance with ASTM E1921 [27], with the exception that the standard does not cover testing of specimens containing shallow cracks. The cracks were created using fatigue pre-cracking at room temperature according to the recommendations in E1921, which resulted in straight crack fronts in all specimens. When pre-cracking the shallow specimens, the crack length was estimated using a strain measurement technique. Testing was carried out in a computer controlled cooling chamber utilizing liquid nitrogen to cool the specimen. The fracture toughness testing was carried out in displacement control with a loading rate corresponding to 1 $\mathrm{MPa}\sqrt{\mathrm{m}}/\mathrm{s}$ during the initial elastic region of the test. The fracture toughness was evaluated from the load line displacement. The J-integral at failure was calculated from the load line displacement (LLD) where the plastic η-factor valid for shallow cracks in SEN(B)-specimens was taken from Faleskog et al. [28].

The cleavage fracture toughness results were interpreted by means of the master curve standard ASTM E1921 [27]. The ductile-to-brittle reference temperature T_0 was evaluated according to that standard. The master curve concept is based on a probabilistic weakest link model for brittle cleavage fracture assuming small-scale yielding conditions and self-similar crack tip fields [29]. The probability of failure at $K_{J\mathrm{c}}$ is expressed by

$$P_f = 1 - \exp\left(-\frac{B}{B_0}\left[\frac{K_{J\mathrm{c}} - K_{\min}}{K_0 - K_{\min}} \right]^4 \right), \quad (1)$$

where B is the thickness of a specimen (or crack front width), B_0 is a reference thickness which is set to 1T = 25.4 mm, $K_{\min}$ is a threshold fracture toughness, and $K_0 = K_0(T, T_0)$ is a temperature dependent reference fracture toughness that is referenced to 100 $\mathrm{MPa}\sqrt{\mathrm{m}}$ for a 1T specimen at T_0. More specifically, K_0 is well described by

$$K_0 = 31 + 77\exp\left(0.019\left[T - T_0\right]\right)\ \mathrm{MPa}\sqrt{\mathrm{m}}. \quad (2)$$

For the master curve to be able to give a good description of a materials cleavage fracture toughness the material itself needs to be homogeneous. In the case of a large degree of scatter due to material inhomogeneity, ASTM E1921 supplies additional methodology of T_0-evaluation so that a conservative estimate of the fracture toughness can be ensured. One example of such methods is the SINTAP-methodology, which now has been included in E1921, where an additional safety factor is included in the evaluation of T_0. Such methods may be needed in the evaluation of the fracture toughness of weld metals, where the scatter may be larger than that of more microstructurally homogeneous base metals. Another example is the case where the material displays a bimodal toughness distribution, where the bimodal master curve [30] can be utilized, which is expressed as

$$P_f = 1 - p_a \exp\left(-\frac{B}{B_0}\left[\frac{K_{Jc} - K_{\min}}{K_0^A\left(T_0^A\right) - K_{\min}} \right]^4 \right) - \left(1 - p_a\right)\exp\left(-\frac{B}{B_0}\left[\frac{K_{Jc} - K_{\min}}{K_0^B\left(T_0^B\right) - K_{\min}} \right]^4 \right). \quad (3)$$

The bimodal master curve requires three parameters that needs to be estimated, where T_0^A and T_0^B corresponds to the reference temperature for each mechanism (mode in the distribution), respectively, and p_a is a probability scaling parameter that defines the contribution of each mechanism.

As the original master curve model is based on self-similar crack tip fields (small-scale yielding, high constraint), it is not capable of handling the effect of loss of constraint. In order to incorporate the effect of constraint, an empirical correction of T_0 by the T-stress is proposed by Wallin [31], [32], as

$$T_0 = T_0^{\text{high constraint}} + \Delta T_0^{\text{constraint}}, \text{ where } \Delta T_0^{\text{constraint}} = A\frac{\Delta T_{\text{stress}}}{\sigma_{\text{y}}}. \quad (4)$$

Here, the difference in T-stress at the limit load between the predicted geometry and the geometry used to determine $T_0^{\text{high constraint}}$ should be used, where $T_0^{\text{high constraint}}$ normally is referred to as T_0, as the standard test method prescribes the use of deeply cracked specimens which produce a state of high constraint. In (4), the factor A is a yield strength dependent parameter that is empirically found to be approximately $\sigma_{\text{y}}/10\,\text{MPa/°C}$ [31] for $\sigma_{\text{y}} > 600$ MPa and constant equal to 40 ˚C [32] when σ_{y} is below 600 MPa. It should be noted that the constraint correction of the master curve is still partially developed for more complex geometries [33].

As the main purpose with this study is to investigate the sensitivity to the constraint effect on the fracture toughness of the thermally aged weld metal from the pressurizer and compare those results to the reference material available, a well-grounded approach is needed. An objective way to compare the constraint sensitivity of two materials is to choose the testing temperatures such that the median of the high constraint fracture toughness coincides. The next step is to conduct low constraint testing at the same temperatures, elucidating potential differences in the constraint effect on the fracture toughness between the two materials.

The testing was therefore conducted in the following steps:

i. Initial test series according to ASTM E1921 to find the reference temperature T_0 for the two materials

ii. use T_0 to determine temperatures where the high constraint fracture toughness will be the same for the two materials

iii. conduct remaining test series, high and low constraint as well as small specimens.

From the test results in step *i.*, T_0 was evaluated to determine the testing temperatures to be used in step *iii*. The testing temperatures that would yield the same high constraint cleavage fracture toughness was chosen to be -50 ˚C for R4PRZ and -90 ˚C for R3RPVH. Both materials were tested in series of 12 specimens in step *iii*.

Alongside the tests for the brittle fracture toughness, tests for the ductile fracture toughness were also conducted. These were carried out at a temperature of 75 ˚C to avoid brittle fracture altogether, i.e. clearly being on the upper shelf. The testing was performed with SEN(B)-specimens with side-grooves to promote uniform growth across the thickness of the specimens. The specimens were extracted from the T-S orientation with dimensions W = 30 mm, B = 15 mm, B_N = 12 mm, and a/W = 0.5, which is the same as used for the specimens in the brittle fracture tests. All testing was conducted in accordance with ASTM E1820 [34]. The J-integral was calculated from the crack mouth opening displacement (CMOD).

2.3. Tensile and hardness testing

Uniaxial tensile testing was also carried out on round bar specimens of both the weld and the base metal. In addition, hardness testing was performed on the weld metal, before and after heat treatments at 430 ˚C and 600 ˚C, respectively. Note that different samples were used for the different temperatures. The hardness tests were performed to investigate the recovery of the ageing induced hardening during heat treatments. Hardness testing according to Vickers with an indentation load of 10 kgf was chosen as the test method. The specimens used were manufactured into blocks measuring 15 mm × 8 mm × 4 mm. An initial grid of indents were made to map out the initial hardness of the two materials, R4PRZ and R3RPVH, were the samples displayed a slight variation of hardness across the surface intended for measurement, as a result of the varying microstructure inherent to the weld. Hardness was also measured across and along the centerline the weld in both materials.

2.4. Atom Probe Tomography and Transmission Electron Microscopy

The nanostructure of the material has been investigated by APT, which was performed in a LEAP 3000X HR from Imago Scientific Instruments. From the results of the study in [21], it was expected that unevenly distributed Ni-Mn-Cu-Si rich clusters would be found. Due to this, large volumes of material were needed to be analysed, and thus laser pulsing was used in addition to voltage pulsed analysis. However, laser pulsing affects the Si position due to surface diffusion [35] and thus both pulsing modes were used. For voltage pulsed analysis, a temperature of 50 K and pulse fraction of 20 % was used. For laser pulsed analysis, the temperature was 30 K and the laser energy 0.3 nJ. In both cases the laser pulse frequency was 200 kHz. The sample preparation was done using a standard two-step electropolishing method [36], finishing with pulsing to get rid of surface oxides. The reconstructions were made in the IVAS 3.6 software, using reconstruction parameters k between 4.0 and 5.3, and evaporation field of 33 V/nm in the case of voltage pulsed analysis and 23 V/nm for laser pulsed analysis. The image compression factor was set to 1.65 for all reconstructions.

The cluster analysis was performed using the maximum separation method (MSM) [37], [38], a method that requires some careful choice of parameters in order to get relevant and comparable results [39], [40]. Cluster parameters were chosen by comparing the data set to a randomised version, and aiming to avoid defining random fluctuations in composition as clusters. Solute elements were chosen to be Cu, Ni, and Mn. The maximum solute atom distance in order for two atoms to be considered being in a cluster, d_{max}, was set to 0.45 nm, and the smallest number of solute atoms defining a cluster, N_{min}, was chosen to 20. Cluster sizes were determined by calculating the number of solute atoms in the clusters, assuming α-Fe body centred cubic structure and a detection efficiency of the LEAP of 37 %. The amount of Fe in the cluster is uncertain, since local magnification effects focus Fe atoms into the clusters during field evaporation [41], [42]. Thus, the 50 % Fe detected in clusters in these APT reconstruction is probably considerably lower in the actual material. Here, the Fe content is excluded from the clusters when calculating the size. This might give a slight underestimation if there is any Fe in the clusters. Cluster compositions were determined using MSM as well. For the number density, clusters on the edge of the analysis were identified and counted as half a cluster. It should be noted that the terms precipitate and cluster is used interchangeably in this paper, as the characterisation method (APT) do not give any crystallographic information.

3. Experimental results

3.1. Fracture toughness tests

In the evaluation of the reference temperature T_0, it was observed that the two materials behaved differently, which was due to the degree of inhomogeneity. The thermally aged R4PRZ displays a larger degree of inhomogeneity and has therefore been evaluated with the more conservative SINTAP-evaluation than that of the reference material R3RPVH, which was evaluated according to the normal procedure of E1921. The deeply cracked specimens of both data sets are shown as a function of testing temperature in Figure 2 together with the master curve predictions based on the respective materials T_0. It is clear that the thermally aged R4PRZ is more brittle than R3RPVH, with a difference in T_0, ΔT_0 = 45 ˚C. Estimating the T_{41J} from the T_0 of R3RPVH by the empirical relation supplied in E1921 ($T_{41J} = T_0 + 24$ ˚C) yields T_{41J} = -54 ˚C, which agrees well with the check-in values for T_{41J} listed in Table 2, giving justification to using R3RPVH as a (fracture toughness) reference to R4PRZ.

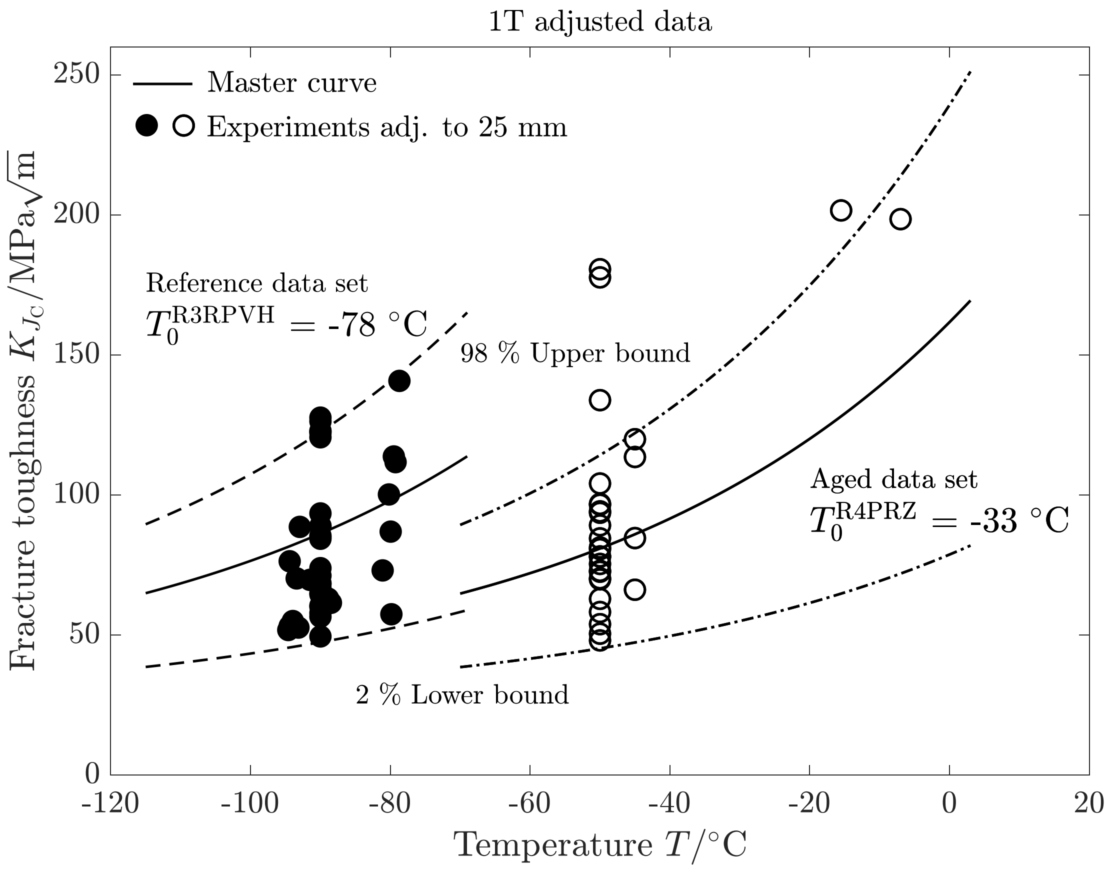

Figure 2. Fracture toughness of individual specimens belonging to both R3RPVH and R4PRZ against testing temperature, and the predicted temperature dependence from the master curve model.

By looking at the ranked probability of the single temperature tests, i.e. the constraint sensitivity tests, it appears that the R4PRZ displays a bimodal toughness distribution as seen in Figure 3, while R3RPVH does not, as seen in Figure 4. The rank probability is here computed as the median rank by Benard's approximation $P_f^i \approx (i - 0.3)/(N + 0.4)$.

Especially noticeable is that the low constraint R4PRZ specimens (*a/W* = 0.1) behave very similar to high constraint R4PRZ specimens (*a/W* = 0.5) at rank probability levels below 0.4, where the fracture toughness essentially coincide (Figure 3). While at higher levels of rank probability, the low constraint R4PRZ specimens (*a/W* = 0.1) is subject to ductile crack growth up to 1 mm prior to brittle failure. Consequently, the scatter in fracture toughness becomes extreme and is found in the range 9.6 kN/m to 785 kN/m.

As seen in Figure 5, the chosen temperatures for the constraint sensitivity tests were appropriate as the resulting fracture toughness of the high constraint specimens (Figure 5 a) is at par for both materials. In Figure 5 (b), the low constraint results for both materials is compared, which clearly shows the difference between the thermally aged R4PRZ and the reference R3RPVH. In Figure 5 (c), a comparison of the fracture toughness of the small specimens is shown, which aligns well, once again displaying the conformity of fracture toughness pertinent to high constraint geometries.

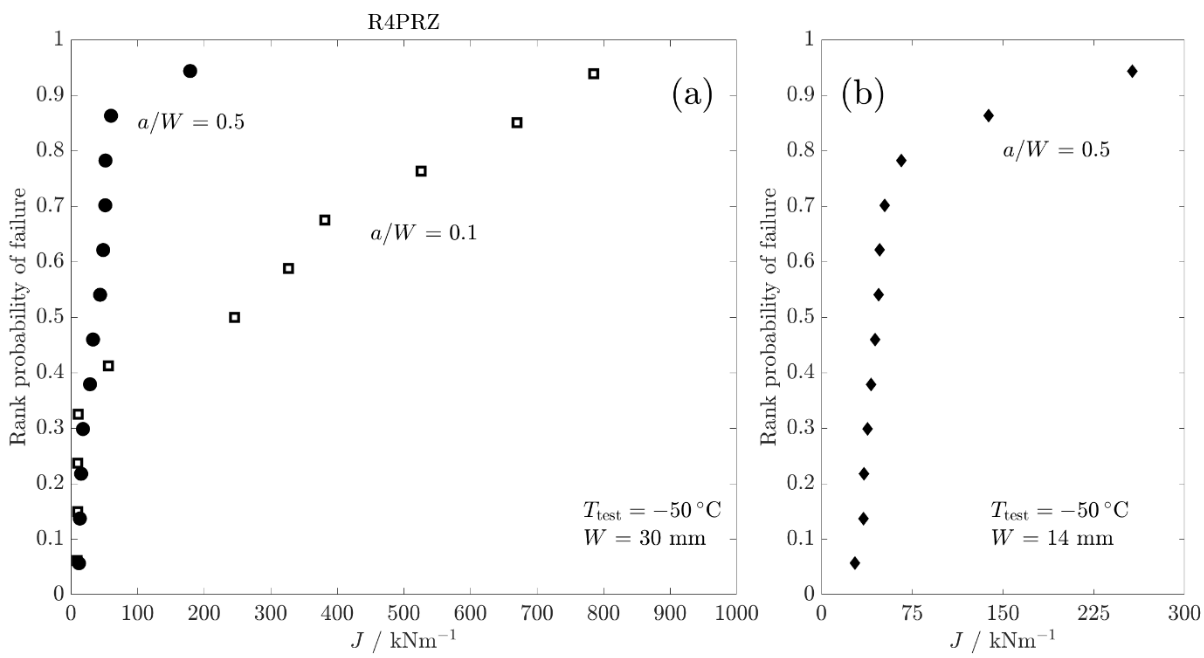

Figure 3. Rank probabilities for the fracture tests of R4PRZ at the test temperature -50 ˚C. (a) Data sets where *W* = 30 mm and *a/W* = {0.5, 0.1}. (b) Data set where *W* = 14 mm and *a/W* = 0.5.

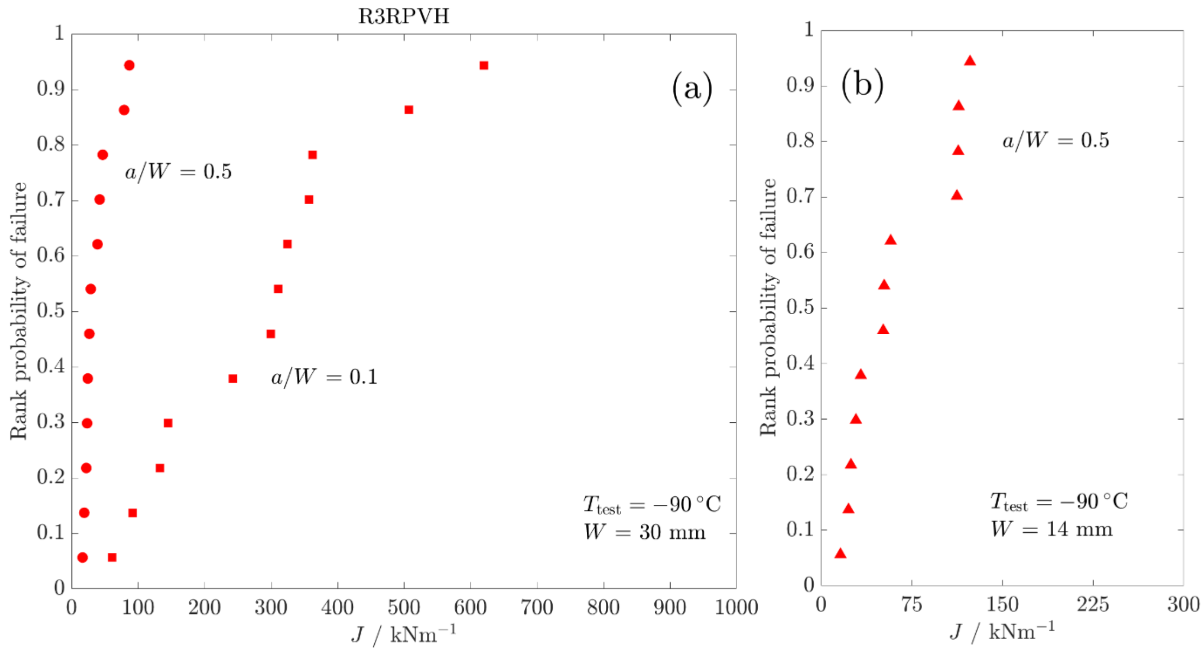

Figure 4. Rank probabilities for the fracture tests of R3RPVH at the test temperature -90 ˚C. (a) Data sets where $W = 30$ mm and $a/W = \{0.5, 0.1\}$. (b) Data set where $W = 14$ mm and $a/W = 0.5$.

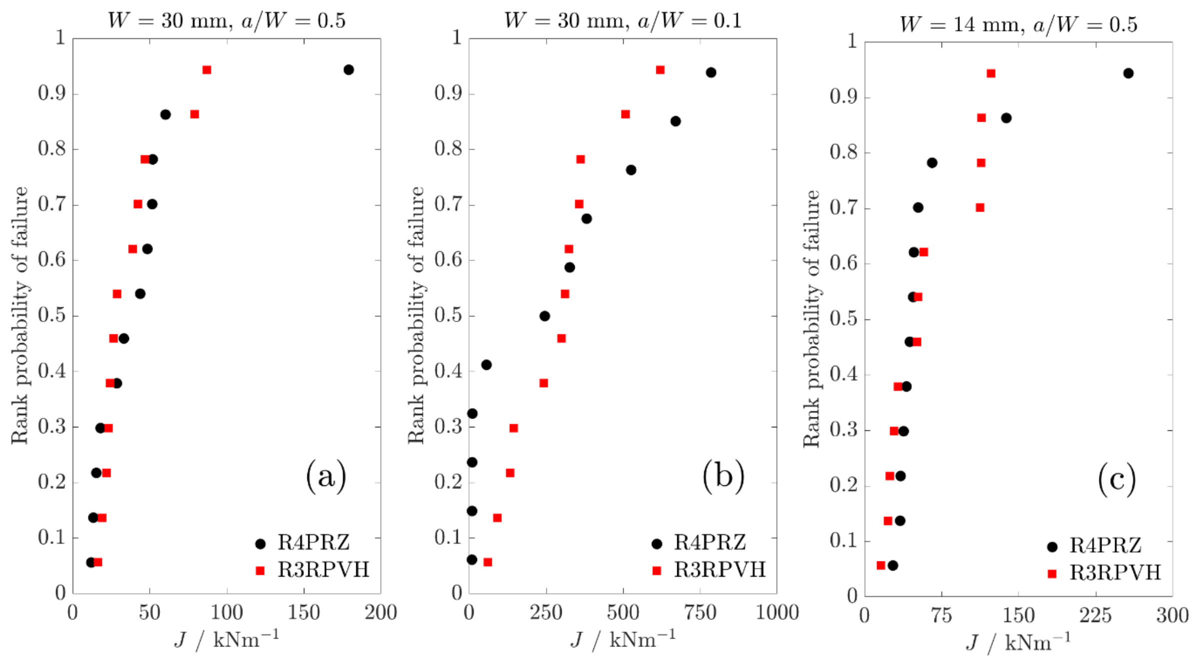

Figure 5. Rank probabilities for the fracture tests of R4PRZ and R3RPVH for comparison of fracture toughness distribution. (a) Data set where $W = 30$ mm and $a/W = 0.5$. (b) Data set where $W = 30$ mm and $a/W = 0.1$. (c) Data set where $W = 14$ mm and $a/W = 0.5$.

Fractography of the single temperature fracture tests presented in Figure 3-Figure 5 reveals that initiation of brittle fracture in the *low toughness specimens* from the thermally aged R4PRZ has occurred by grain boundary cracking. Here, the fracture surfaces are consistently riddled with intergranular facets in direct connection to the crack front. This with no evidence of brittle fracture initiation from a second phase particle, as is commonly observed for cleavage fracture in ferritic steels. Observations of the *higher toughness specimens* unveils transgranular features and subsequently fracture initiation from second phase particles in tandem with intergranular features. For instance, low toughness brittle fracture appears to be solely associated with intergranular fracture while at higher levels of toughness, a mixture of both inter- and transgranular fracture appears to be the underlying cause of brittle fracture. Some examples of this is shown in Figure 6 and Figure 7 where low and high toughness specimens containing deep and shallow cracks are shown. For clarity, a low magnification image (uppercase) is associated with one of higher magnification (lowercase) per level of fracture toughness shown.

Turning to the fracture morphology of the reference material R3RPVH. In this material, virtually unaffected by ageing, transgranular fracture is dominating the entire specimen population with few exceptions, where traces of intergranular fracture can be found in low toughness specimens. It should be noted that R3RPVH is not a perfect reference material, since it has been in operation during a significant number of years, however at a lower temperature and shorter time than R4PRZ.

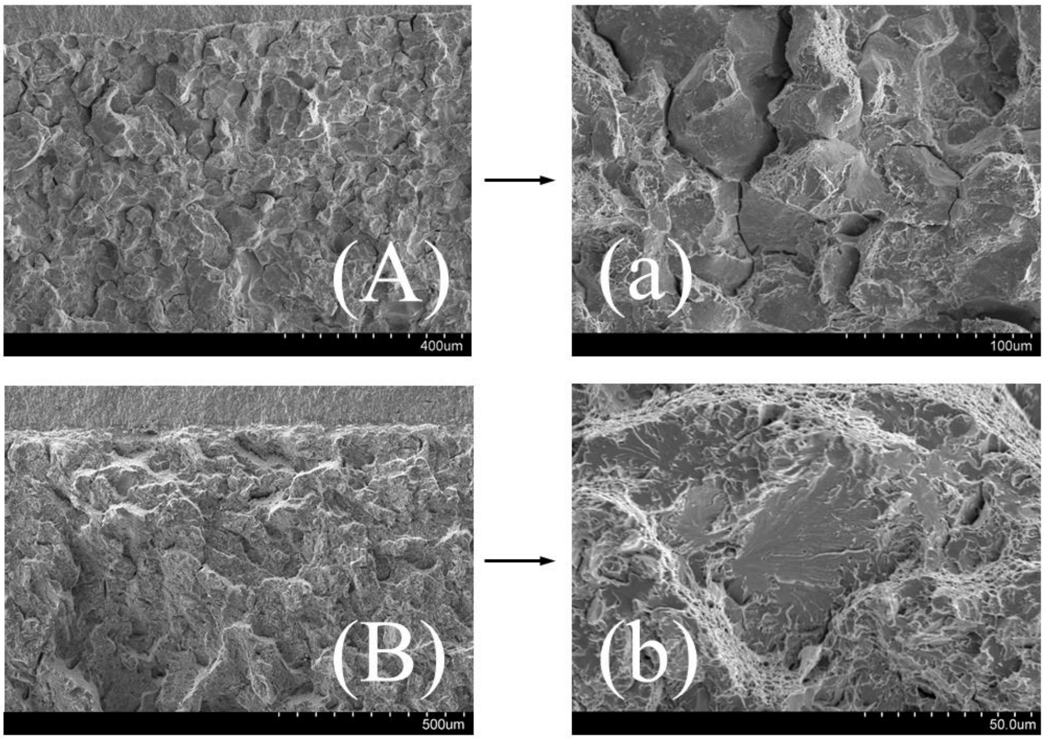

Figure 6. Fractography of deeply cracked specimens (a/W = 0.5) from the R4PRZ data set. Specimen {(A), (a)} fractured at a *low* toughness of K_{JC} = 52 $\mathrm{MPa}\sqrt{\mathrm{m}}$, displays intergranular fracture, note secondary cracks in (a). Specimen {(B), (b)} fractured at a *higher* toughness of K_{JC} = 108 $\mathrm{MPa}\sqrt{\mathrm{m}}$, displays transgranular fracture, probable initation point in (b).

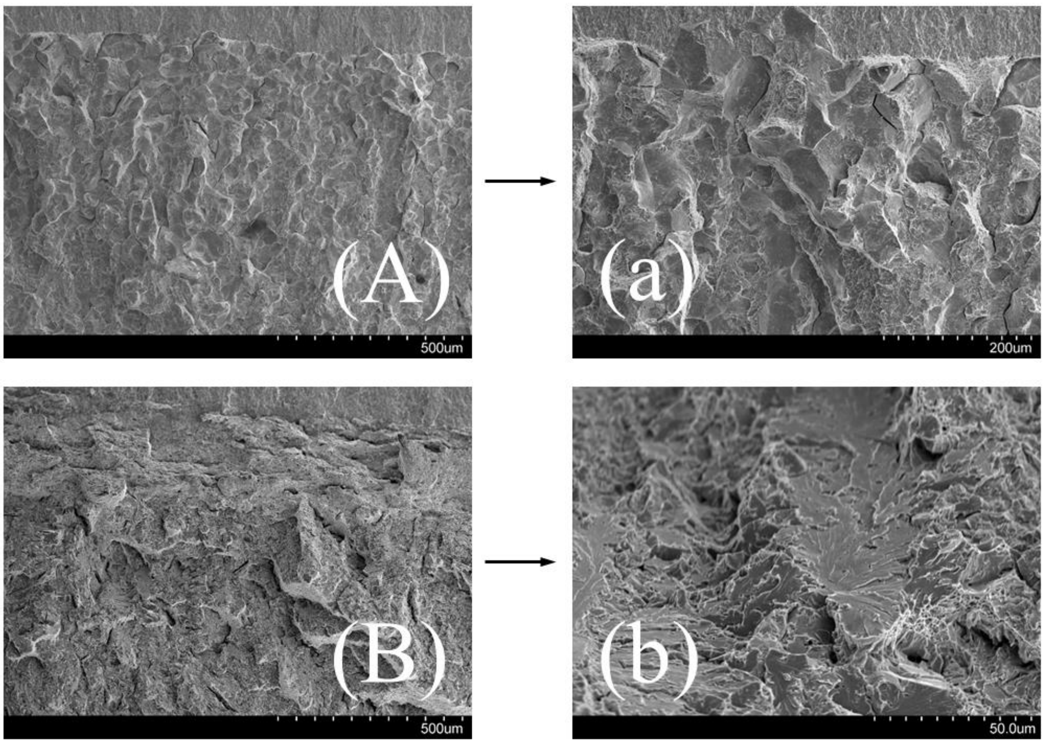

Figure 7. Fractography of shallowly cracked specimens (a/W = 0.1) from the R4PRZ data set. Specimen {(A), (a)} fractured at a *low* toughness of K_{JC} = 50 $\mathrm{MPa}\sqrt{\mathrm{m}}$, displays intergranular fracture, note secondary cracks in (a). Specimen {(B), (b)} fractured at a *higher* toughness of K_{JC} = 270 $\mathrm{MPa}\sqrt{\mathrm{m}}$, displays transgranular fracture, probable initation point in (b).

The results from the ductile fracture toughness testing is shown in Figure 8, where both the force-CMOD relation and the J_R-behavior for the two materials is shown. From these results it can be clearly distinguished that the ductile initiation fracture toughness J_{IC} = 337 kN/m is the same for both materials while the resistance to crack growth differs such that the thermally aged R4PRZ offers less resistance to crack growth after approximately 1 mm of growth.

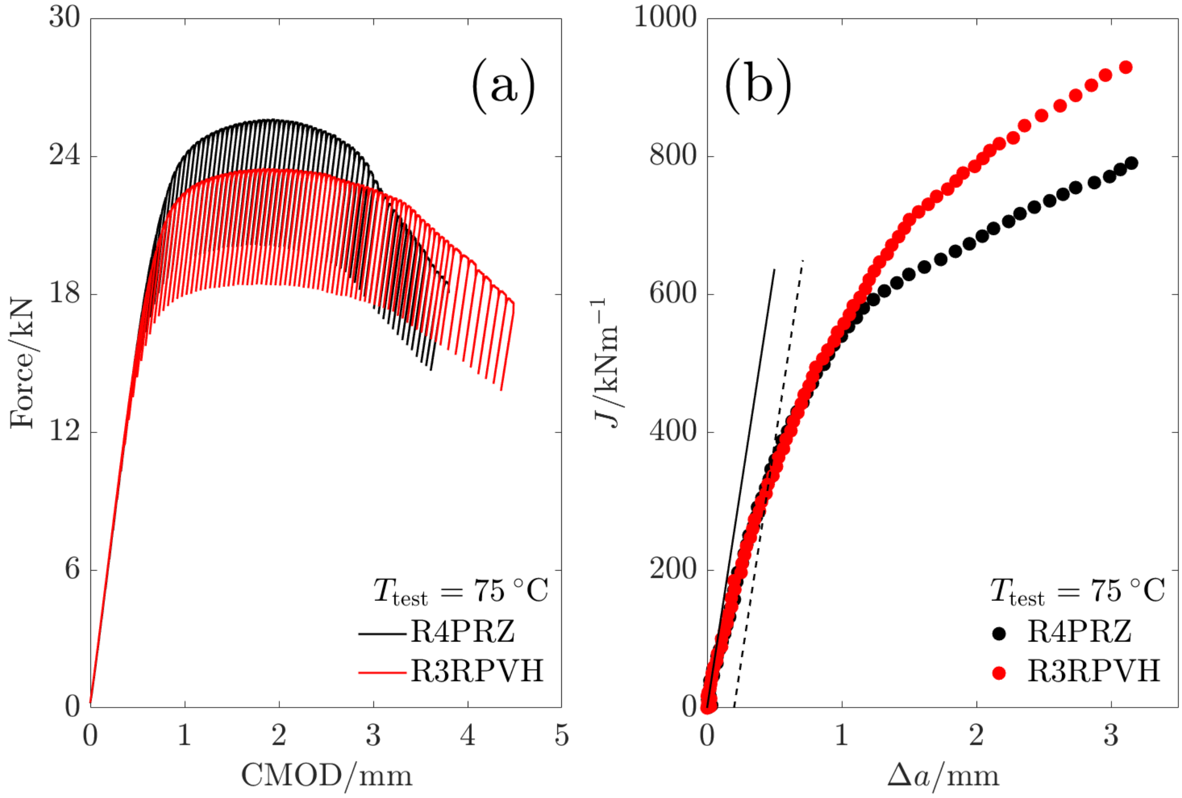

Figure 8. Results from ductile fracture toughness testing. (a) Force-CMOD relation. (b) J-Δa relation.

3.2. Tensile and hardness tests

Figure 9 shows a selection of the tensile tests that were carried out in this investigation. Figure 9 (a) shows the tensile results at the testing temperatures pertinent to the constraint sensitivity fracture tests and it can be seen that the yield and ultimate tensile strength are virtually the same. Figure 9 (b) displays the tensile results at room temperature, where it can be seen that the thermally aged R4PRZ appears to be slightly stronger than the reference R3RPVH. The tensile testing indicates that both materials are subjected to some hardening due to operation as the yield strength from the current investigation is higher than that of the check-in testing, a comparison is shown in Table 3.

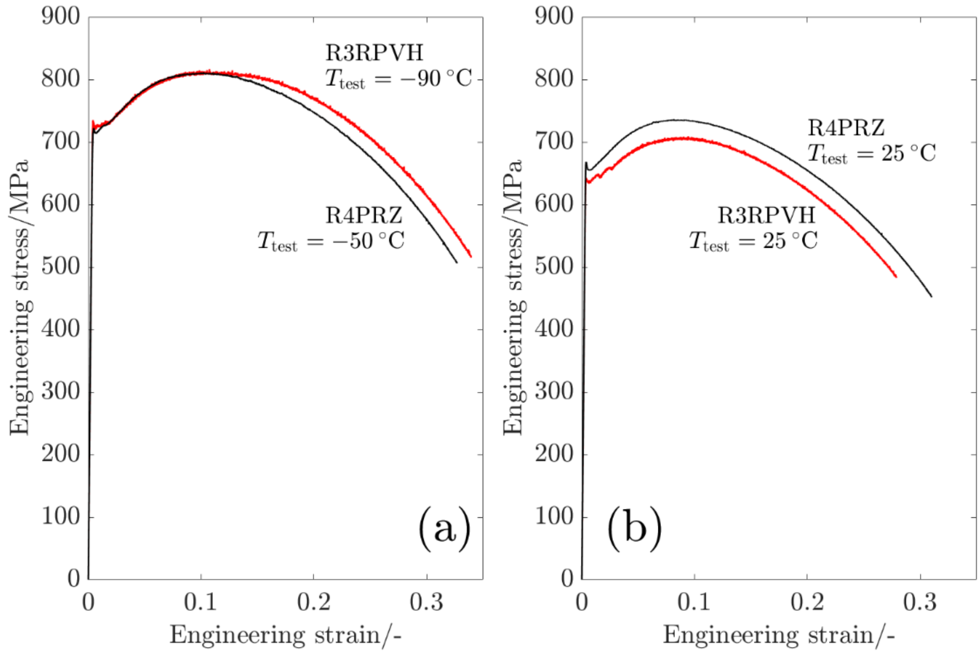

Figure 9. Tensile tests of R4PRZ and R3RPVH. (a) At constraint sensitivity test temperatures. (b) At room temperature.

Table 3. Comparison between check-in yield strength and the results obtained in this investigation.

R_{p02}/MPa	Check-in	Current	Difference
R4PRZ	579	656	77
R3RPVH	575	637	62

The results from the Vickers hardness tests are shown in Figure 10, where the hardness measured across and along the weld centerline in one of the R4PRZ and R3RPVH SEN(B)-specimens used for brittle fracture testing is plotted. It can clearly be seen that the hardness corresponds well with the results from the tensile tests in Figure 9 for the two materials. For the hardness tests combined with heat treatments, annealing at 430 ˚C gave no change in hardness for times up to 50 h. However, annealing at 600 ˚C gave the results shown in Figure 11, where normalized hardness is presented for both materials against annealing time. The error bars represents the range in hardness from the measurements after annealing. The initial hardness of the specimens used in Figure 11 can be represented by 248 kgf/mm^2 and 254 kgf/mm^2, which decreased to 220 kgf/mm^2 and 213 kgf/mm^2 after 25 h of annealing for R4PRZ and R3RPVH respectively. It should be noted that a significant variability in hardness exists in the specimens, hence the wide range of the error bars.

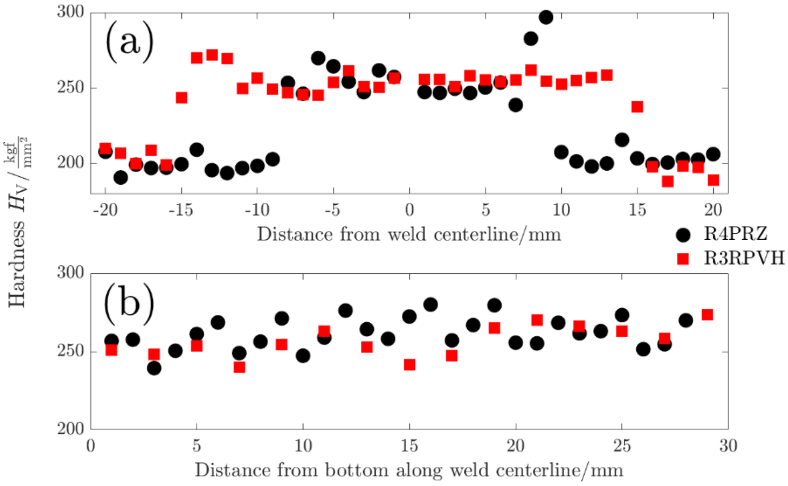

Figure 10. Hardness measured on SEN(B)-specimens of R4PRZ and R3RPVH. (a) Shows the hardness across the weld centerline, from base metal to weld metal into base metal. (b) Shows the hardness along the weld centerline.

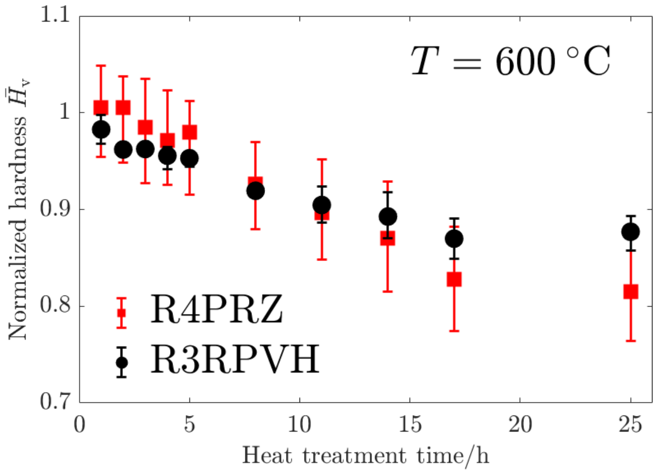

Figure 11. Hardness of R4PRZ and R3RPVH against heat treatment time. Error bars represents the range in hardness measurement at each annealing.

3.3. Master curve analysis of single temperature fracture tests

By estimating the parameters of the bimodal master curve relevant to the single temperature fracture tests of R4PRZ, the results in Figure 12 are obtained. When the three parameters are estimated for the high constraint specimen in Figure 12 (a), it appears to yield a consistent prediction of the size effect in Figure 12 (c). However, there is no ambiguous manner in which a constraint adjustment can be made to reliably predict the experimental rank probabilities of the low constraint specimen in Figure 12 (b). Therefore, the results presented in Figure 12 (b) corresponds to the low constraint specimen are without corrections for loss of constraint. Furthermore, the bimodal master curve prediction in Figure 12 (b) was based on a new set of parameters that were estimated to fit the experimental results shown in this graph. Thus, one set of bimodal parameters cannot be used to capture the experimental results of both the high and low constraint specimens displayed in Figure 12. It should be noted that the master curve methodology, unimodal and bimodal, is based on self-similar crack tip fields related to a stationary crack, while the results in Figure 12 (b) are subject to significant ductile crack growth prior to brittle failure. This will have an impact on the accuracy of the master curve with regards to parameter estimation and model predictions around and above the ductile initiation fracture toughness, J_{IC} = 337 kN/m.

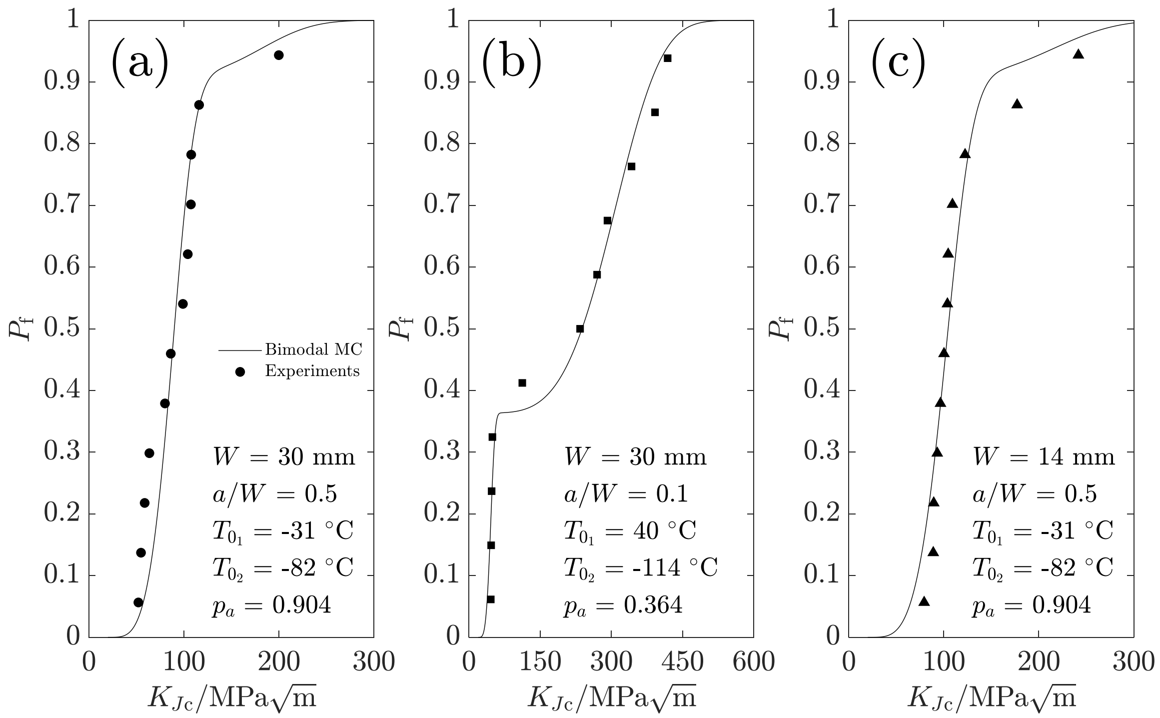

Figure 12. Comparison of predicted failure probabilities (solid lines) from the bimodal master curve with rank probabilities for the experimental fracture tests pertaining to R4PRZ (symbols). (a) Data set where W = 30 mm and a/W = 0.5. (b) Data set where W = 30 mm and a/W = 0.1. (c) Data set where W = 14 mm and a/W = 0.5. Note, no constraint correction using e.g. T-stress has been used, the low constraint data has been used for both prediction and parameter estimation.

In Figure 13, master curve predictions of the probability of failure of the fracture tests of the reference material, R3RPVH are shown. Clearly, there is no need to use the bimodal master curve to describe the fracture toughness distribution of the reference material. The results presented in Figure 13 (a) corresponding to the low constraint specimens (a/W = 0.1) are successfully constraint corrected using Eq. (4) where $A = \sigma_y / 10\,\mathrm{MPa/°C}$.

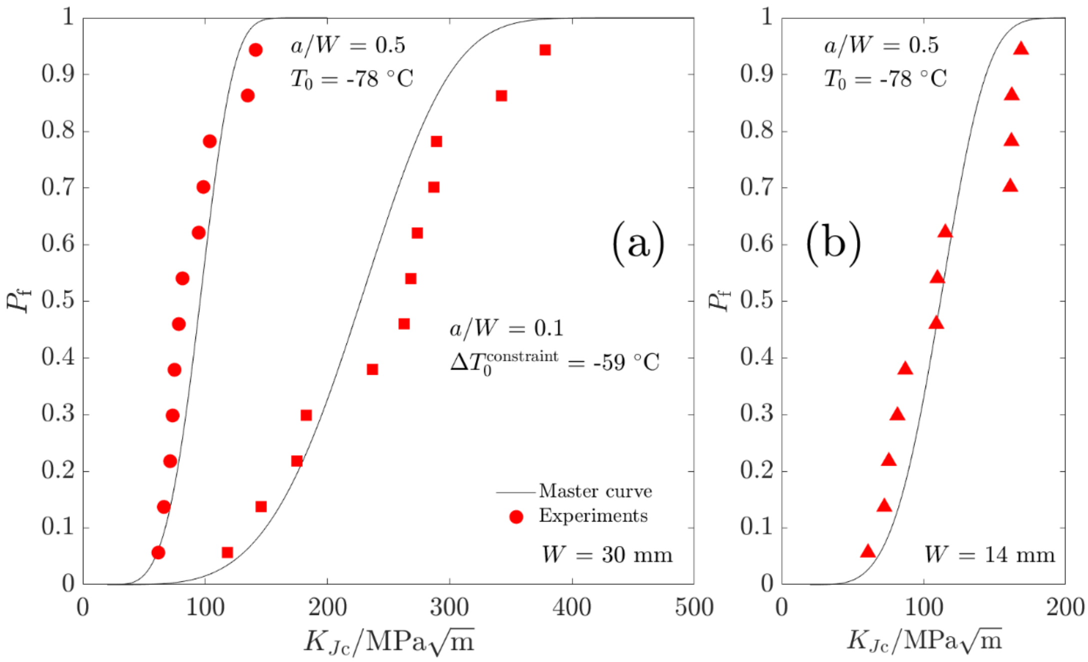

Figure 13. Comparison of predicted failure probabilities (solid lines) from the (unimodal) master curve with rank probabilities for the experimental fracture tests pertaining to R3RPVH (symbols). (a) Data set where W = 30 mm and a/W = 0.5 and data set where W = 30 mm and a/W = 0.1. (c) Data set where W = 14 mm and a/W = 0.5. Note, T_0 has been subject to constraint correction using the T-stress for the low constraint specimens, a/W = 0.1 presented in (a).

3.4. Atom Probe Tomography and Transmission Electron Microscopy

Regarding the results from the APT investigation, the chemical compositions from APT can be seen in Table 4. The standard deviation between the different analyses of the same material is given, as APT is a local method and the welded material is chemically heterogeneous on the considered length scale. The average Ni content of the R4PRZ is slightly higher than that of R3RPVH. The average compositions (at.%) are generally close to the nominal composition (given in wt.% in Table 1).

Table 4. Chemical compositions as measured by APT. The standard deviation between the runs are given as an estimate of the local variation in composition. N and S are omitted due to their overlaps with Si^{2+} and O, respectively, in the APT spectrum.

At. %	R4PRZ	R3RPVH
C	0.03±0.03	0.03±0.01
Si	0.42±0.09	0.47±0.04
P	0.02±0.01	0.01±0.01
V	0.004±0.003	0.002±0.001
Cr	0.13±0.01	0.05±0.01
Mn	1.33±0.15	1.35±0.07
Co	0.01±0.01	0.02±0.01
Ni	1.69±0.58	1.36±0.08
Cu	0.05±0.01	0.05±0.01
Mo	0.12±0.07	0.19±0.07
Fe	Bal.	Bal.

In the R4PRZ material, clusters were found using APT, see Figure 14. The analyzed material was found to be heterogeneous; some of the smaller analyses did not contain any features whereas some contained many. Solute clusters containing Ni, Mn, Cu, and Si, were found in the reconstruction seen in Figure 14. Some of these appear to have nucleated on carbonitrides. The carbonitrides contain V, Cr, Mo and some Mn, and some are found on dislocations, decorated with Mo and C. As seen in the figure, not all carbonitrides contain all elements. The reconstruction in Figure 14 also contain a boundary layer with Mo, C, some Ni, Si and Mn, and a few clusters/precipitates, out of which two appear to contain Cu and two does not.

A difficulty when analyzing the clusters and carbonitrides was the overlap in the mass spectrum at 32.5 Da. Both $^{65}Cu^{2+}$ and VN^{2+} have peaks here in the voltage pulsed analyses. This was handled by using the peak at 31.5 to identify Cu^{2+} atoms, comparing with the local natural abundance of ^{65}Cu and ^{63}Cu. An example of this is shown in Figure 15, where the top precipitate is a carbonitride and the peak at 32.5 is mainly VN^{2+}. The 32.5 peak atoms then mainly coincide with the V atoms, whereas there are Cu atoms spread out outside the carbonitride. In the lower cluster, that consist of mainly Ni, Mn, Si and Cu, the 32.5 peak is mainly $^{65}Cu^{2+}$, and the ions coincide with the $^{63}Cu^{2+}$ atoms at 31.5 Da. In laser pulsed runs the field is lower and thus most of the Cu evaporate as 1+ ions [43]. In this case, the overlap problem is less prominent as VN still evaporates as VN^{2+}.

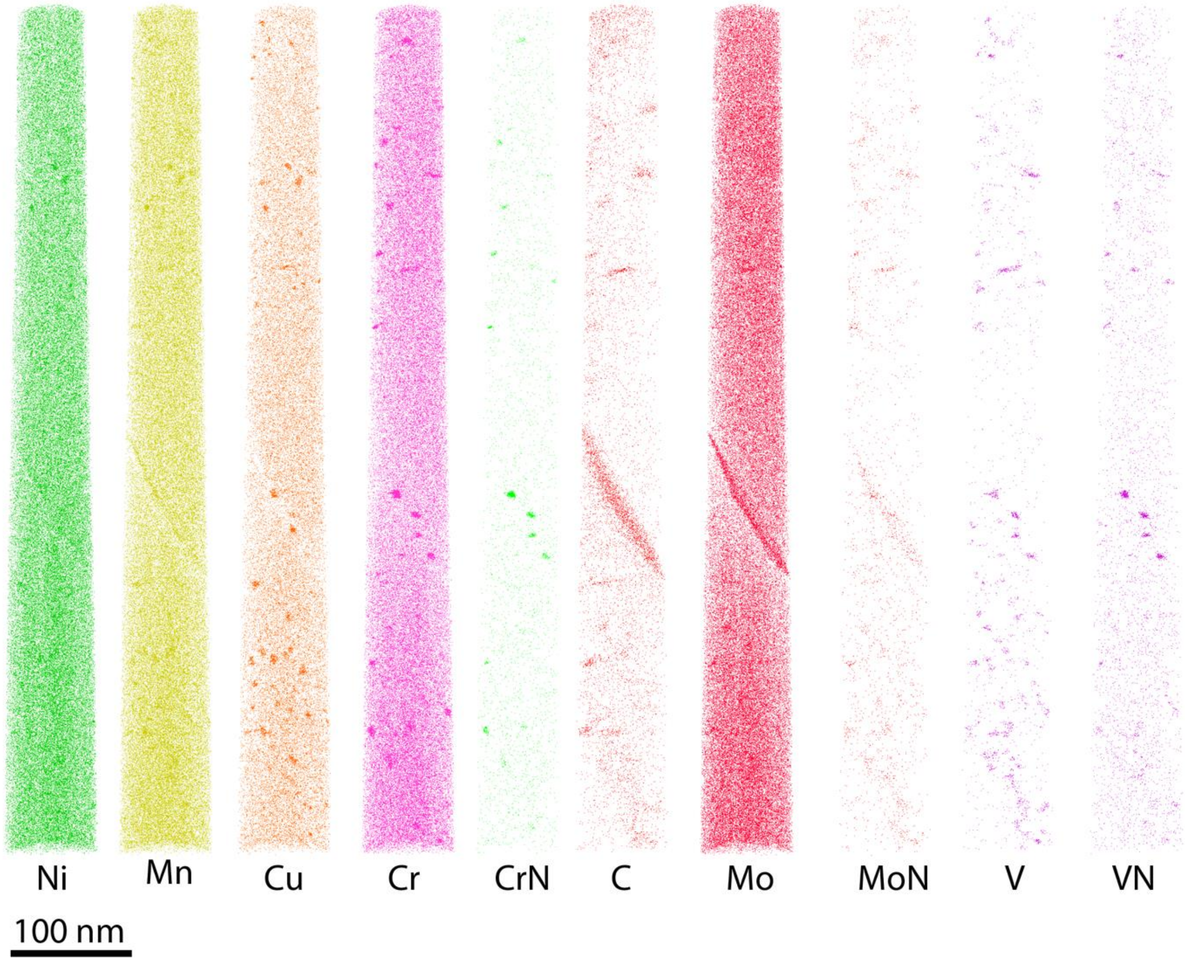

Figure 14. APT reconstruction of thermally aged R4PRZ material. Only ions that are not randomly distributed are shown. This analysis was run in laser pulsed mode.

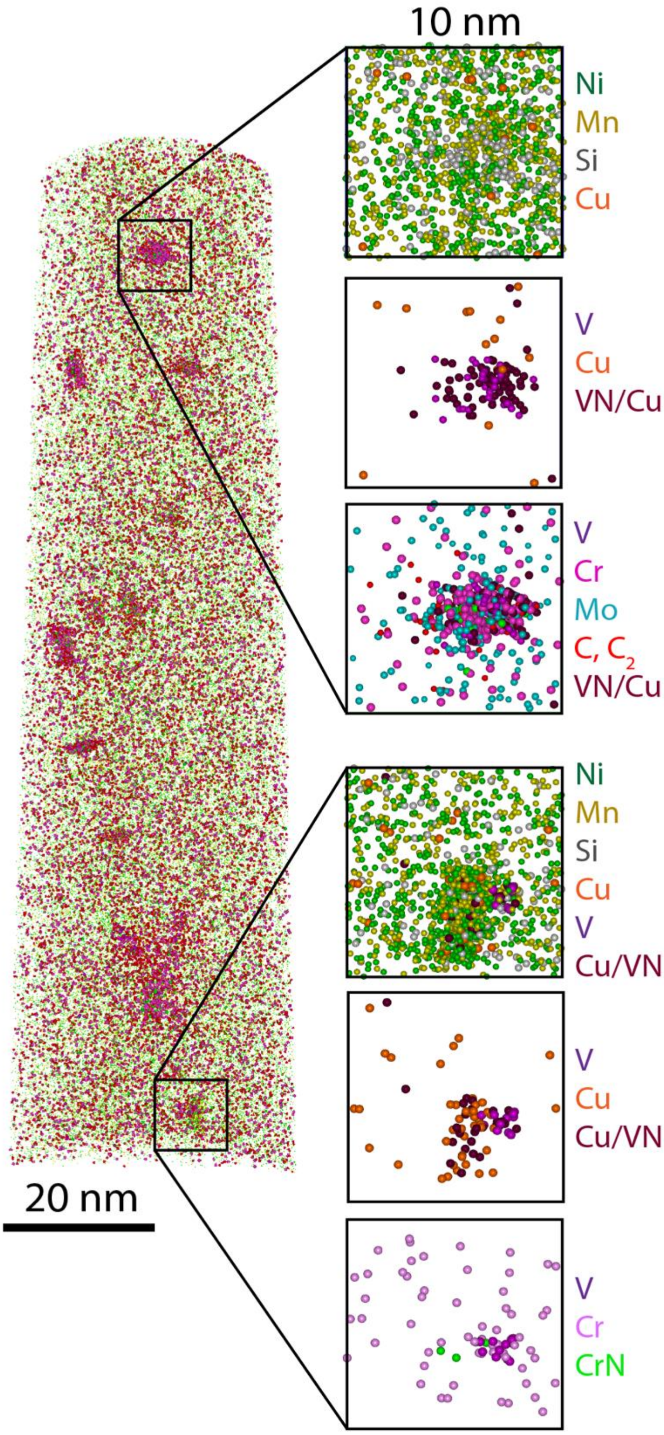

Figure 15. Atom probe reconstruction of the thermally aged R4PRZ material. Two precipitates are cut out in boxes of 10×10×10 nm^3, with different elements shown. The top V and Cr-rich carbonitride does not contain any Ni or Cu, and only small amounts of Mn. The ions marked VN/Cu are mainly VN. The lower precipitate contain mainly Ni, and Mn, and some Cu. There is also some V in one part of the precipitate. Most of the Cu/VN ions are probably Cu. This analysis was run in voltage pulsed mode.

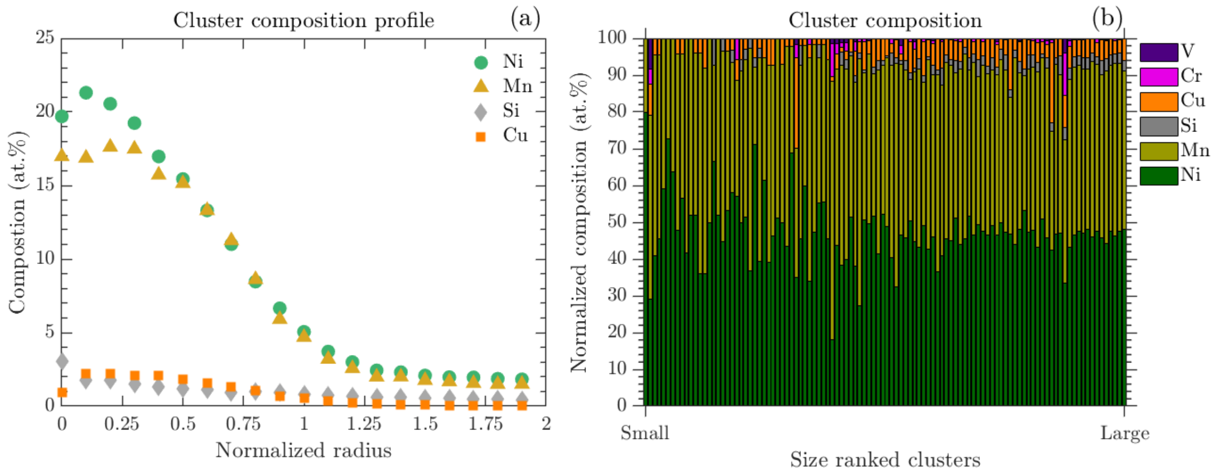

Figure 16. The composition profile, and the cluster composition cluster by cluster, normalized by Fe in R4PRZ. The composition profile is not normalized in terms of composition, but the radius is. 0 correspond to the cluster center, and 1 to the edge of the cluster. The cluster composition cluster by cluster is sorted in increasing size.

In Figure 16, the normalized composition profile and the individual cluster compositions of one analysis are shown. The clusters contain mainly Ni and Mn, and smaller amounts of Cu and Si. It was found that the cluster Cu content varied between the different analyses, and that the example in Figure 16 is low in Cu. The clusters have similar composition within the same analysis. Many of the clusters contain some V or Cr. The average size of the Cu-rich clusters was also varying between the analyses, but the average was found to be 2.1±0.3 nm, and the number density $0.13 \pm 0.05 \cdot 10^{23}$ /m^3.

The reference material from the RPVH of Ringhals R3, R3RPVH, was also analysed using APT. One reconstruction can be found in Figure 17. In general, this material contained a lower density of small carbonitrides than the pressurizer. Still, some were found, and also Mo and C enriched dislocations, and boundaries. In Figure 17 a Mo-rich carbide is sitting on the boundary.

Interestingly, occasional clusters containing Cu, Ni, and Mn were found in the R3RPVH material. In Figure 17, one is present on the boundary layer. In other reconstructions, a few clusters were found on dislocations. The number density of the precipitates was very low, and they were not homogeneously distributed.

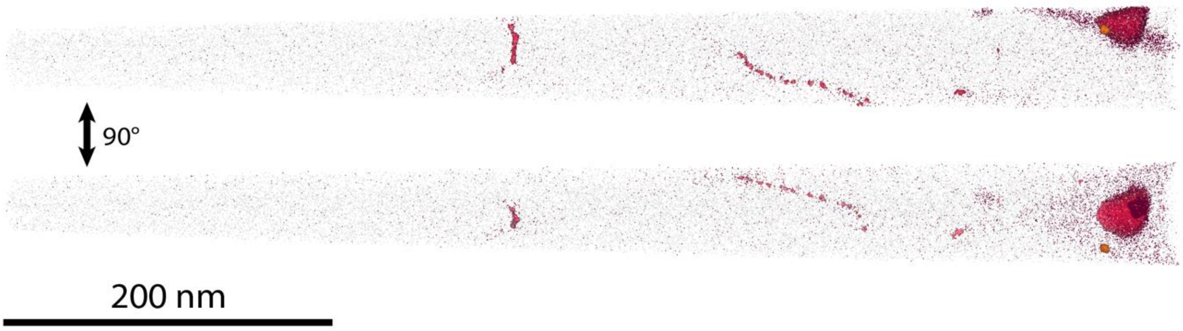

Figure 17. APT reconstruction of the RPV head. Red isoconcentration surfaces correspond to Mo 1.9%, orange to Cu 1%, and brown dots are C atoms. A few dislocations are visible as well as a boundary layer containing a Mo-rich carbide and a Cu-rich precipitate. The outline of the analysis is shown in grey. The reconstruction is turned 90°.

4. Discussion

The in-service thermal ageing of the pressurizer weld metal from Ringhals unit 4 appears to manifest through both hardening and non-hardening embrittlement mechanisms. That is, both by an increase in yield strength and by a weakening of the grain boundaries of the material. The effects of the embrittlement due to thermal ageing are profound in that they both give a significant change in the reference temperature T_0 and affects the fracture toughness distribution. As seen in Figure 3-5 the comparison between the fracture toughness distributions of R4PRZ and R3RPVH reveals that there are some apparent differences at conditions that should be equal in terms of the high constraint fracture toughness. The most notable being that the low constraint specimens of R4PRZ shows a very wide range in the test data, where the most brittle specimens display fracture initiation through intergranular fracture and the tougher specimens appears to experience brittle fracture initiation from both grain boundaries and second phase particles, where the latter appears to bring out transgranular fracture features.

The toughness distribution of the R4PRZ appears to be bimodal where the bimodality has its origin in the multiple initiation mechanisms. This indicates that failure initiated from a grain boundary is weaker than that of failure initiated from a second phase particle in this material. The upper part of the distribution for the R4PRZ appears to be tougher than that of R3RPVH, which is likely an effect of ductile crack growth that occurs prior to the final brittle fracture.

For describing the toughness distribution of the thermally aged R4PRZ, the bimodal master curve is required and appears to be able to describe the material well under conditions of high constraint. The reference material R3RPVH is well described by the standard master curve, i.e. the *unimodal* model. However, the transition between the high and low constraint geometries is not trivial. For the case of R3RPVH, the correction of T_0 for the low constraint $a/W = 0.1$ appears to work well using Wallin's empirical relation [31]. But, a constraint correction for the bimodal master curve that ideally should be used to describe the R4PRZ is currently ambiguous due to the complex interactions of the initiation mechanisms and the number of parameters included in the model.

Separating the effects from hardening and non-hardening contributions to the change in fracture toughness is not clear. From the fractography of the thermally aged R4PRZ, the effects of non-hardening embrittlement can be distinguished from the presence of intergranular features. The hardening contribution was elucidated by the combination of hardness tests and heat treatments. From the measurements presented in Figure 11, the hardness in both materials can be seen to decrease by 12-18 % which is similar to the difference between the yield strengths obtained in the current investigation and the check-in data. It should also be noted that the decrease in hardness is to a level judged to be relevant to the as-manufactured hardness of the weld. This implies that there appears to be a hardening effect present in both the R4PRZ and the R3RPVH materials, i.e. hardening due to thermal ageing.

Concerning the ductile fracture tests presented in Figure 8, the fracture toughness plotted against crack growth aligns well for crack growth up to ~1 mm, thereafter it deviates so that the R4PRZ has less resistance than R3RPVH. This is accompanied with a change in the fracture surface appearance where the morphology changes notably. A possible explanation would be that the crack grows into a different part of the microstructure, which presents different requisites for void growth and coalescence, the main operating mechanism for ductile crack growth in these materials. As an example, if the crack starts growing in a zone with a reheated microstructure (small equiaxed grains), it is likely that the ductile fracture resistance will change once the crack grows into an as-welded zone (elongated dendritic grains), or vice versa.

The obvious material to compare the APT-results of the R4PRZ material with is the pressurizer weld analysed by APT by the authors in [21] and [44]. This weld comes from the same component, but is slightly different in terms of composition. The clusters containing Cu, Ni, Mn, and Si are relatively similar in appearance. The Cu content is higher in the clusters reported in [21] and [44], but the measured Cu content is also higher in that weld (0.10 at. % compared to the 0.05 at. % in the weld in this paper). The lower Cu content makes the core-shell structure (Cu-rich core) less prominent in the clusters of this paper. The size and number density of the two materials are within the estimated errors considering the heterogeneous distribution.

As mentioned earlier, the terms cluster and precipitate are used interchangeably in this paper, as APT does not provide enough crystallographic information to reveal the crystal structure of these small clusters/precipitates. Generally, bcc Cu-clusters in α-Fe are believed to transform into 9R precipitates when they have a diameter of at least around 4 nm, and into fcc at larger sizes [45], [46]. Here, the Ni and Mn content of the clusters is high, and thus question is what type of precipitate is formed, and at which diameter.

The most significant difference from the other weld of the same pressurizer is the amount of small carbonitrides. In the other material, occasional V and Cr-containing carbonitrides were found. They were also found in the reference material used in that paper and in the Ringhals RPV weld metal [47]. It is assumed that the carbonitrides are present before ageing, and are thus not affecting the shift of mechanical properties in a direct way. They appear to act as nucleation point for the Cu-rich clusters, as many of them are found in connection to each other (see Figure 14-16). The higher number of carbonitrides does, however, not seem to give a significant increase in the number of Ni-Mn-Si-Cu clusters as the number density of 0.13 10^{23} $/m^3$ here is close and within the uncertainty to the 0.16 10^{23} $/m^3$ as measured in [21]. Also, there are carbonitrides were Cu, Ni, Mn and Si have not precipitated/clustered, see Figure 14 and 15.

The fact that Ni-Mn-Cu-Si clusters could be found in the RPV head material that was used as reference material is interesting. The diffusion of these elements in α-Fe is very low at the relevant temperature (310-315 °C). However, no such clusters were found in similar un-aged reference materials used by the authors in similar high Ni and Mn, low Cu weld metals [21], [47].

5. Conclusions

The effects of embrittlement due to thermal ageing on the weldments from a pressurizer of a Swedish nuclear power plant, more specifically the effect of ageing on the constraint sensitivity of the fracture toughness has been investigated and compared to a reference material. Testing revealed a $\Delta T_0 = 45$ °C between the materials, indicating a considerable embrittlement. The thermally aged material displays a bimodal fracture toughness distribution, which is significantly pronounced at low constraint, and is due to brittle fracture being initiated from weakened grain boundaries as well as second phase particles. To describe the fracture toughness distribution, the bimodal master curve is needed and no constraint correction for the low constraint specimens can unambiguously be made. The reference material is well described by the unimodal master curve and the constraint effect is well predicted within the same framework.

The nanostructure of both materials is characterized using atom probe tomography where in-homogeneously distributed solute clusters of Ni-Mn-Cu-Si situated on dislocations and on carbonitrides, which are also present within the material.

A hardening due to thermal ageing is apparent in both the studied materials and is investigated using uniaxial tensile tests as well as hardness tests in combination with heat treatments. After annealing at 600 ˚C for 25 h it appears that the ageing induced hardening is restored, most likely due to dissolution of solute clusters formed due to thermal ageing.

Acknowledgements

The Swedish Radiation Safety Authority (SSM) and the Swedish Centre for Nuclear Technology (SKC) are acknowledged for their finanical support. Ringhals AB is acknowledged for supplying the material that was used in the experimental investigation. Jenny Roudén is greatly acknowledged for her support in this study and for constructive comments on the manuscript.

References

[1] L. Debarbis, B. Acosta, A. Zeman, S. Pirfo och P. Moretto, ”Ductile-to-brittle transition temperature of thermally segregated WWER-1000 base metal,” *International Journal of Microstructure and Materials Properties,* vol. 2, pp. 326-338, 2007.

[2] B. A. Gurovich , A. A. Chernobaeva, D. Yu Erak, E. A. Kuleshova, D. A. Zhurko, V. B. Papina, M. A. Skundin och D. A. Maltsev, ”Chemical composition effect on VVER-1000 RPV weld metal thermal ageing,” *Journal of Nuclear Materials,* vol. 465, pp. 540-549, 2015.

[3] A. A. Chernobaeva, E. A. Kuleshova, B. A. Gurovich, D. Yu Erak, O. O. Zabusov, D. A. Maltsev, D. A. Zhurko, V. B. Papina och M. A. Skundin, ”Thermal ageing effects of VVER-1000 weld metal under operation temperature,” i *Fontevraud 8*, Avignon, 2014.

[4] Y. I. Shtrombakh, B. A. Gurovich, E. A. Kuleshova, D. A. Maltsev, S. V. Fedotova och A. A. Chernobaeva, ”Thermal ageing mechanisms of VVER-1000 reactor pressure vessel steels,” *Journal of Nuclear Materials,* vol. 452, pp. 348-358, 2014.

[5] P. Joly, F. Roch och C. Primault, ”Effect of thermal ageing on properties of pressure vessel low alloy steel,” i *Proceedings of the ASME 2013 Pressure Vessels and Piping Conference*, Paris, 2013.

[6] R. Pelli och J. Forstén, ”Effect of thermal ageing on impact ductility of the nuclear pressure vessel steel SA533B and its weld metal,” *Theoretical and Applied Fracture Mechanics,* vol. 8, pp. 25-31, 1987.

[7] J. Kameda och Y. Nishiyama, ”Combined effects of phosphorus segregation and partial intergranular fracture on the ductile-brittle transition temperature in structural alloy steels,” *Materials Science and Engineering A,* vol. 528, pp. 3705-3713, 2001.

[8] A. Andreiu, A. Pineau, P. Joly, F. Roch och D. Ryckelynck, ”Influence of P and C intergranular segregation during manufacturing and ageing on the fracture toughness of nuclear pressure vessel steels,” *Procedia Materials Science,* vol. 3, pp. 655-660, 2014.

[9] S. G. Druce, G. Gage och J. G., ”Effect of ageing on properties of pressure vessel steels,” *Acta Metallurgica,* vol. 34, nr 4, pp. 641-652, 1986.

[10] I. A. Vatter, C. A. Hippsley och S. G. Druce, ”Review of Thermal Ageing Data and its Application to Operating Reactor Pressure Vessels,” *International Journal of Pressure Vessels and Piping,* vol. 54, pp. 31-48, 1993.

[11] C. Naudin, J. M. Frund och A. Pineau, ”Intergranular fracture stress and phosphorus grain boundary segregation of a Mn-Ni-Mo steel,” *Scripta Materialia,* vol. 40, nr 9, pp. 1013-1019, 1999.

[12] C. L. Briant och S. K. Banerji, ”Intergranular failure in steel: the role of grain boundary composition,” *International Metal Reviews,* pp. 164-199, 1978.

[13] C. J. McMahon, ”Intergranular Fracture in Steels,” *Materials Science and Engineering,* vol. 25, pp. 233-239, 1976.

[14] M. Guttmann, ”Equilibrium segregation in a ternary solution: a model for temper embrittlement,” *Surface Science,* vol. 53, pp. 213-227, 1975.

[15] M. Guttmann, ”Temper Embrittlement and Ternary Equilibrium Segregation,” *Materials Science and Engineering ,* vol. 42, pp. 227-232, 1980.

[16] S. K. Banerji, C. J. McMahon och H. C. Feng, ”Intergranular Fracture in 4340-Type Steels: Effects of Impurities and Hydrogen,” *Metallurgical Transactions A,* vol. 9A, pp. 237-247, 1978.

[17] D. F. Stein, ”Reversible temper embrittlement,” *Annual Review of Materials Research,* vol. 7, pp. 123-153, 1977.

[18] M. K. Miller, K. A. Powers, R. K. Nanstad och P. Efsing, ”Atom probe tomography characterizations of high nickel, low copper surveillance RPV welds irradiated to high fluences,” *Journal of Nuclear Materials,* vol. 437, pp. 107-115, 2013.

[19] P. D. Styman, J. M. Hyde, D. Parfitt, K. Wilford, M. G. Burke, C. A. English och P. Efsing, ”Post-irradiation annealing of Ni-Mn-Si-enriched clusters in a neutron-irradiated

RPV steel weld using Atom Probe Tomography," *Journal of Nuclear Materials,* vol. 459, pp. 127-134, 2015.

[20] K. Lindgren, M. Boåsen, K. Stiller, P. Efsing och M. Thuvander, "Evolution of precipitation in reactor pressure vessel steel welds under neutron irradiation," *Journal of Nuclear Materials,* vol. 488, pp. 222-230, 2017.

[21] K. Lindgren, M. Boåsen, K. Stiller, P. Efsing och M. Thuvander , "Cluster formation in in-service thermally aged pressurizer welds," *Journal of Nuclear Materials,* vol. 504, pp. 23-28, 2018.

[22] J. M. Hyde, G. Sha, E. A. Marquis, A. Morley, K. B. Wilford och T. J. Williams, "A comparison of the structure of solute clusters formed during thermal ageing and irradiation," *Ultramicroscopy,* vol. 111, pp. 664-671, 2011.

[23] P. D. Styman, J. M. Hyde, K. Wilford, A. Morley och G. D. W. Smith, "Precipitation in long term thermally aged high copper, high nickel model RPV steel welds," *Progress in Nuclear Energy,* vol. 57, pp. 86-92, 2012.

[24] P. D. Styman, J. M. Hyde, K. Wilford och G. D. W. Smith, "Quantitative methods for the APT analysis of thermally aged RPV steels," *Ultramicroscopy,* vol. 132, pp. 258-264, 2013.

[25] P. D. Styman, J. M. Hyde, K. Wilford, D. Parfitt, N. Riddle och G. D. W. Smith, "Characterisation of interfacial segregation to Cu-enriched precipitates in two thermally aged reactor pressure weld steels," *Ultramicroscopy,* vol. 159, pp. 292-298, 2015.

[26] H.-W. Viehrig, M. Housaka, D. Kalkhof och H.-J. Schindler, "Fracture mechanics characterisation of reactor pressure vessel multi-layer weld metal," *International Journal of Pressure Vessels and Piping,* Vol. %1 av %2135-136, pp. 36-51, 2015.

[27] ASTM International, "E1921 Standard Test Method for Determination of Reference Temperature, T0, for Ferritic Steels in the Transition Range," ASTM International, West Conshohocken, 2019.

[28] J. Faleskog, M. Kroon och H. Öberg, ”A probabilistic model for cleavage fracture with a length scale - parameter estimation and predictions of stationary crack experiments,” *Engineering Fracture Mechanics,* vol. 71, pp. 57-79, 2004.

[29] K. Wallin, ”The scatter in KIC-results,” *Engineering Fracture Mechanics,* vol. 19, nr 6, pp. 1085-1093, 1984.

[30] K. Wallin, P. Nevasmaa, A. Laukkanen och T. Planman, ”Master Curve analysis of inhomogeneous ferritic steels,” *Engineering Fracture Mechanics,* vol. 71, pp. 2329-2346, 2004.

[31] K. Wallin, ”Quantifying T-stress controlled constaint by the master curve transition temperature T0,” *Engineering Fracture Mechanics,* vol. 68, pp. 303-328, 2001.

[32] K. Wallin, Fracture Tougness of Engineering Materials - Estimation and Application, Croydon: EMAS Publishing, 2011.

[33] M. Boåsen, M. Stec, P. Efsing och J. Faleskog, ”A generalized probabilistic model for cleavage fracture with a length scale - Influence of stress state and application to surface cracked experiments,” *Engineering Fracture Mechanics,* vol. 214, pp. 590-608, 2019.

[34] ASTM International, ”E1820 Standard Test Method for Measurement of Fracture Toughness,” ASTM International, West Conshohocken, 2019.

[35] J. M. Hyde, M. G. Burke, B. Gault, D. W. Saxey, P. Styman, K. B. Wilford och T. J. Williams, ”Atom probe tomography of reactor pressure vessel steels: an analysis of data integrity,” *Ultramicroscopy,* vol. 111, nr 6, pp. 676-682, 2011.

[36] M. K. Miller, Atom Probe Tomography: Analysis at the Atomic Level, Academic/Plenum Publishers: 2000, 200.

[37] J. M. Hyde och C. A. English, ”An Analysis of the Structure of Irradiation induced Cu-enriched Clusters in Low and High Nickel Welds,” i *Materials Research Society Symposium*, Boston, 2000.

[38] D. Vaumousse, A. Cerezo och P. J. Warren, ”A procedure for quantification of precipitate microstructures from three-dimensional atom probe data,” *Ultramicroscopy,* vol. 95, pp. 215-221, 2003.

[39] Y. Dong, A. Etienne, A. Frolov, S. Fedotova, K. Fujii, K. Fukuya, C. Hatzoglou, E. Kuleshova, K. Lindgren, A. London, A. Lopez, S. Lozano-Perez, Y. Miyahara, Y. Nagai, K. Nishida, B. Radiquet, D. K. Schreiber, N. Soneda, M. Thuvander, T. Toyama, J. Wang, F. Sefta, P. Chou och E. A. Marquis, ”Atom Probe Tomography Interlaboratory Study on Clustering Analysis in Experimental Data Using the Maximum Separation Distance Approach,” *Microscopy and Microanalysis,* vol. 25, nr 2, pp. 356-366, 2019.

[40] K. Lindgren, K. Stiller, P. Efsing och M. Thuvander, ”On the Analysis of Clustering in an Irradiated Low Alloy Reactor Pressure Vessel Steel Weld,” *Microscopy and Microanalysis,* vol. 23, nr 2, pp. 379-384, 2017.

[41] E. A. Marquis och J. M. Hyde, ”Applications of atom-probe tomography to the characterization of solute behaviours,” *Materials Science and Engineering: R: Reports ,* vol. 69, nr 4-5, pp. 37-62, 2010.

[42] P. D. Edmondson, C. M. Parish och R. K. Nanstad, ”Using complimentary microscopy methods to examine Ni-Mn-Si-precipitates in highly-irradiated reactor pressure vessel steels,” *Acta Materialia,* vol. 134, pp. 31-39, 2017.

[43] D. R. Kingham, ”The Post-Ionization of Field Evaporated Ions: a Theoretical explanation of Multiple Charged States,” *Surface Science,* vol. 116, pp. 273-301, 1982.

[44] K. Lindgren, M. Boåsen, K. Stiller, P. Efsing och M. Thuvander, ”Thermal ageing of low alloy steel weldments from a Swedish nuclear power plant - the evolution of the microstructure,” i *Fontevraud 9*, Avignon, 2018.

[45] A. Deschamps, M. Militzer och W. J. Poole, ”Comparison of Precipitiation Kinetics and Strengthening in an Fe-0.8%Cu Alloy and a 0.8% Cu-containing Low-carbon Steel,” *ISIJ International ,* vol. 43, pp. 1826-1832, 2003.

[46] P. J. Othen, M. L. Jenkins och G. D. W. Smith, ”High-resolution electron microscopy studies of the studies of the structure of Cu precipitates in α-Fe,” *Philosophical Magazine A,* vol. 70, pp. 1-24, 1994.

[47] K. Lindgren, M. Boåsen, K. Stiller, P. Efsing och M. Thuvander, ”Evolution of precipitation in reactor pressure vessel steel welds under neutron irradiation,” *Journal of Nuclear Materials,* vol. 488, pp. 222-230, 2017.

[48] R. Xing, D. Yu, G. Xie, Z. Yang, X. Wang och X. Chen, ”Effect of thermal aging on mechanical properties of a bainitic forging steel for reactor pressure vessel,” *Materials Science and Engineering A,* vol. 720, pp. 169-175, 2018.

Effect of weld microstructure on brittle fracture initiation in a thermally aged boiling water reactor pressure vessel head weld metal

N. Hytönen, Z. Que, P. Arffman, J. Lydman, P. Nevasmaa, U. Ehrnstén, P. Efsing

September 8, 2020

Abstract

The effect of the weld microstructure and inclusions on the brittle fracture initiation is investigated in a thermally aged ferritic high-nickel weld of a reactor pressure vessel head from a decommissioned nuclear power plant. As-welded regions consist mainly of acicular ferrite and reheated regions mainly of polygonal ferrite. The fractographic examination of Charpy V-notch impact toughness specimens reveal large inclusions (0.5–2.5 µm) at the brittle fracture primary initiation sites. Higher impact energies were measured for specimens where brittle fracture initiates from a smaller inclusion or an inclusion further from the V-notch. The density, geometry and chemical composition of the primary initiation inclusions were investigated. The brittle fracture crack initiated as a microcrack either within the multiphase oxide inclusions or from the debonded interfaces between the uncracked inclusions and weld metal matrix. The primary fracture site can be determined in all specimens tested in the lower part of the transition curve, at and below 41 J reference impact toughness energy, but not above, due to the change of the fracture mechanism, and hence the changes in the fracture appearance.

Keywords: Reactor pressure vessel, Brittle fracture, Weld microstructure, Thermal ageing

1 Introduction

The structural integrity of the reactor pressure vessel (RPV) in a nuclear power plant is of utmost importance. During operation, the RPV is subjected to thermal loading and neutron irradiation, which can cause embrittlement and shift the ductile-to-brittle transition temperature (DBTT) of ferritic steel weld with body-centred cubic (bcc) crystal structure towards higher temperatures [1]. The embrittlement is monitored using surveillance programmes, which state and predict the embrittlement and ensure the safe margin towards brittle fracture. These programmes use either Charpy V-notch (CVN) impact and/or fracture toughness test specimens. Welds are typically more critical in terms of irradiation induced embrittlement than base materials. The embrittlement of RPV steels and weld metals have been extensively studied [2, 3, 4, 5, 6, 7, 8], and numerous investigations are ongoing.

Understanding microstructural factors affecting brittle fracture initiation and how this may be influenced by thermal ageing and/or irradiation, is important for an improved mechanistic comprehension of brittle fracture and embrittlement. The first theories about the brittle fracture initiation mechanism were introduced by Griffith [9]. In this classical description of the problem, a microcrack is assumed to initiate within a brittle particle when the stress has exceeded a critical value. The microcrack propagates from the broken particle and develops into a macrocrack. However, it has been shown that the microcrack can also be initiated at the interface between the secondary particle and matrix due to debonding [10]. The stress concentration in a particle is, though, always greater than that at the interface [10]. The weakest link model for initiation at a particle was introduced first by Weibull [11, 12], and later modified by Beremin [13]. These models describe the relationship between the particle size and the probability for brittle fracture initiation [2, 14, 15, 16, 17]. Bowen et al. [18] concluded that the carbides in a martensitic base material were the primary initiators of brittle fracture, while Hein et al. [19] noted a difference between RPV base materials and weld metals, where inclusions were the primary initiators. Investigations on thermally aged weld metal and steels at higher temperatures have concluded that thermal ageing changes the initiation of brittle fracture from a particle to intergranular (IG) fracture [20, 21]. Thus, more data is needed on the role of microstructure on brittle fracture initiation, which can also be used for further development of models for brittle fracture [20].

Weld metals contain secondary particles of different types and sizes. Nickel (Ni), manganese (Mn) and silicon (Si) form complex inclusions, which promote the formation of acicular ferrite. Acicular ferrite is the desired weld microstructure resulting in good toughness properties [22, 23, 24]. However, RPV -operating conditions are known to promote embrittlement due to increased clustering and embrittlement during irradiation [3, 4, 25, 26]. Thermal ageing at 350 ℃ for 27 years of high-Ni weld metal in a pressurizer has been observed to cause increase of the DBTT [3] and clustering [27], and initiation of the low toughness fracture as IG fracture. The single-phase inclusions, such as simple oxides and sulphides (e.g. Al_2O_3 MnO, MnS), cannot nucleate acicular ferrite. The nucleation on an inert surface is a heterogeneous process, where the interfacial energy is a major controlling factor [28]. Hence, complex multiphase inclusions are more effective nucleation sites [24]. Furthermore, the mechanism for acicular ferrite nucleation is dependent on the surface area of the inclusions, hence the intermediate sized inclusions or small inclusions with a higher density promote effectively the acicular ferrite nucleation [29]. The oxide inclusions are treated as brittle particles that fulfil the Griffith criterion of brittle fracture initiation. The particle may act brittle due to the intrinsic crystal structure or due to preceding small defects within the inclusion. Therefore, the inclusion is likely to crack in the presence of plastic strain and further initiate a cleavage fracture. In case of more ductile oxy-sulphides, the matrix debonding can induce cracking within the material and cause further fracture. The characterisation of the inclusions of the investigated weld metal is essential for understanding the brittle fracture initiation mechanisms [30].

The investigated RPV weld metal is from a decommissioned boiling water reactor, which had been operated for 23 effective full power years at 288 ℃. The investigated weld metal is high in Ni and Mn contents. The same weld metal is used in several reactors, and has been investigated earlier concerning e.g. using surveillance material [4, 20, 31, 32]. This investigation is part of larger programmes BREDA and BRUTE including mechanical testing and microstructural characterisation on both RPV head and beltline materials. The main objective of the project is to verify surveillance results using RPV material from a decommissioned nuclear power plant, but also to gain a better mechanistic insight. The objective of this study is to improve understanding on factors affecting brittle fracture by characterising RPV head weld metal removed from a decommissioned RPV, subjected to thermal ageing, but not to irradiation, concerning microstructure, CVN brittle fracture initiation and fracture primary inclusion initiators.

2 Materials and Methods

The material investigated is from the decommissioned Barsebäck unit 2 boiling water reactor. The reactor was in operation for 23 effective full power years at 288 ℃. Cylinder shaped trepans were extracted from the RPV head weld and used for mechanical tests and microstructural characterisation. The investigated weld metal was manufactured using submerged arc welding (SAW) method while the last ~16 mm of the ~70 mm thick weld was made using manual metal arc welding (MMA) due to geometrical factors. The trepans were machined into smaller sections and plates, from which the investigated specimens were cut. The investigated filler materials, Phoenix-Union S3NiMo in the SAW and Oerlicon Tenacito 65 in the MMA weld, are high in Ni and Mn. The chemical composition of the weld by optical emission spectrometry is presented in Table 1.

Table 1: Chemical composition of the weld metal according to the optical emission spectrometry.

wt.%	C	Mn	Ni	Si	Mo	Cr	S	P	Cu	Al	Ti	Co
SAW weld	0.057	1.43	1.48	0.15	0.41	0.03	0.007	0.008	0.060	0.024	0.003	0.020
MMA weld	0.037	1.38	1.22	0.25	0.37	0.03	0.007	0.007	0.004	0.002	0.004	0.018

2.1 Optical microscopy

The weld solidification microstructure, heat-affected zone (HAZ) and the base material were characterised using Zeiss Axio Observer 7 inverted optical microscope to observe and distinguish the different phases and microstructural features. The metallography specimens were polished and etched with 3% Nital solution (HNO3 + ethanol). The multipass weld microstructure is examined through the wall thickness, including samples from both the inner wall side with SAW weld and the outer wall side with MMA weld, as seen in Figure 1. Macro- and microhardness measurements (HV10, HV1 and HV0.3) were performed to exhibit the relation between microstructure and hardness.

The location of the investigated microstructure, i.e., as-welded or reheated region was determined from cross-sections prepared as close as possible to the initiation site after the fractography.

2.2 Inclusion analysis

The density, geometry and chemical composition of inclusions in SAW weld microstructure was investigated using Genesis Software by the energy dispersive X-ray spectrometry (EDS) with 10 keV at current density of 3 nA. An automated feature-sizing analysis was used for the size distribution as the inclusions are recognized automatically through a pre-set thresholds

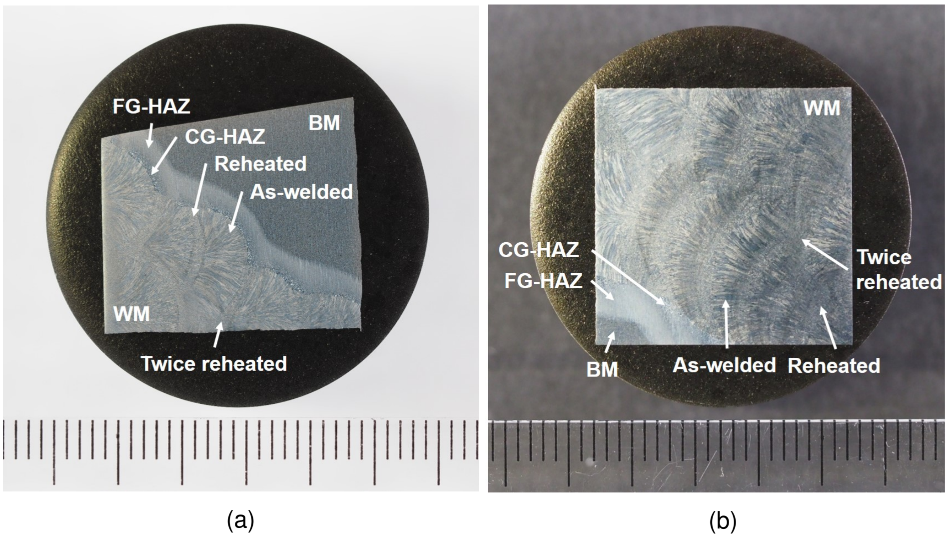

Figure 1: Specimens for characterisation of the investigated weld. a) Specimen from the inner wall side welded with SAW method. b) Specimen from the outer wall side welded with MMA method. Different metallurgical regions are indicated with arrows: base material (BM), weld metal (WM), fine-grained (FG) and coarse-grained (CG) HAZ. The scale has a line spacing of 1 mm.

to the image brightness histogram. Statistical chemical analysis was performed using Genesis Chem, where the point analysis was automatically taken from the centroid of each recognized particle.

The inclusion analysis for the as-welded and reheated regions was done with an imaging field that covers an area of 75 µm × 57 µm on an image resolution of 2048 px, giving a pixel size of 35 nm. Since 2 px is the minimum size for the features to be recognised as an inclusion, a sufficiently identified minimum inclusion size is 70 nm. 1339 inclusions (from 8 fields) and 960 inclusions (from 9 fields) were analysed for as-welded and reheated zones, respectively.

The analysis on the potential brittle fracture primary inclusions with larger size (>0.35 µm) was done with an imaging field covering an area of 217.4 µm × 169.8 µm on an image resolution of 2048 px, giving a pixel size of 106 nm. 100 fields were examined, where 9398 inclusions were analysed with a total scanned area of 3.69 mm^2.

2.3 Charpy V-notch impact toughness testing

The CVN impact toughness specimens were tested according to the standard SFS-EN ISO-148-1:2016 [33]. The tests were performed using a Zwick RKP450 instrumented pendulum with automatic temperature control and feeding system. The pendulum has a 2 mm striker with the nominal impact energy of 300 J. Instrumented strain gauges in the striker tip measure the impact force, which is compared to the deflection in terms of the pendulum angle. The frictional loss measured regularly for free swings and estimated individually for each test gives consistently a loss of 1.0–1.3 J.

Standard specimens have dimensions of 55 mm × 10 mm × 10 mm. The specimens for the CVN impact toughness test were cut at one-quarter depth from the inner surface, with the notch in the middle of the weld. The orientation of the CVN specimens is T-S, differing from the recommended T-L orientation [34]. In the weld structure, the L is the longitudinal direction of welding around the RPV while S is the building direction of a multipass weld.

The transition curve was formed by the transition temperature reference points determined at impact toughness energies of 28 J, 41 J, and 68 J, on a tanh-curve with lower shelf impact energy conservatively set at 2 J and upper shelf estimated as the mean of completely ductile tests. The first test was performed at the ambient temperature and the following temperatures were selected according to the development of the transition curve.

2.4 Fractographic examination

The fracture surfaces of nine CVN specimens with brittle-like fracture appearance from the lower shelf of the transition curve were investigated using the scanning electron microscope (SEM) Zeiss Crossbeam 540. The characterisation focused on the primary initiation site of the fracture and their surrounding area. The distance of the initiation location was measured from the V-notch for further evaluation of the triaxial stress state.

The aim of the analysis is to identify the features and local chemical composition differences at, or adjacent to, the fracture initiation site that have had an impact on the fracture behaviour. Semi-quantitatively chemical composition of the primary fracture area and initiation site were obtained using an EDAX Octane Plus EDS. The topography of the fracture surface inevitably affects the EDS mapping. However, semi-quantitative results revealed the different composition of the particles compared to the surrounding weld, enabling the comparison with results from the inclusion analysis.

3 Results

3.1 Microstructure

The multipass weld is built by weld beads of average height of 4 mm in SAW and 3 mm in MMA weld parts with reheated regions of approximate 1 mm height. The HAZ is uniform throughout the weld, which can be divided into fine-grained (FG) and coarse-grained (CG) regions. The weld microstructure is shown in Figure 2. The epitaxial grain growth begins from the CG-HAZ across the fusion line in the preferred crystallographic direction $\langle 100 \rangle$ and inwards to the weld, as shown in Figure 2a. The acicular ferrite forms into the parent austenite grains during the solidification of the weld bead. The majority of the dendritic weld beads consists of intragranularly nucleated acicular ferrite with small fractions of grain boundary ferrite between the dendrites as seen in Figure 2b. Acicular ferrite has typical fine basket-weave structure which differs significantly from the pre-eutectoid grain boundary ferrite observed as light-coloured elongated areas.

In a multipass welding, the heat input from the consecutive layers impact the microstructure of the as-welded region by refining the dendritic grains through recrystallisation. The reheated microstructure aligns the fan-shaped weld bead of the new weld layer. The reheated microstructure is shown in Figure 2c, where the microstructure mainly consists of polygonal ferrite. Polygonal ferrite appears light-coloured areas in the microstructure without a particular shape. No significant differences in the microstructure were seen between the SAW and MMA welds. Only few larger TiC particles were observed in the MMA weld, which may be due to impurities from the welding process. Additionally, in the MMA HAZ region a few martensite grains were observed.

The Vickers hardness results measured on 10 kg load through wall thickness are shown in Figure 3 which obtain an average hardness of 210$\pm$5 HV10. The lower hardness up to 12 mm from the inner wall is due to the thermal effect from the cladding process. There is no difference between the two welding methods as indicated in the plots. The HV1 was measured over the fusion line, indicating a highest hardness peak at the CG-HAZ region. According to the hardness measurements, i.e., HV10 and HV1, no large areas of hardened microstructure were found, since the size of the martensitic grains were smaller compared to that of the indents.

3.2 Inclusion analysis

The secondary particles in the as-welded and reheated microstructural regions were investigated separately on the metallography specimen. The analyses include the inclusion distribution and geometry analysis (size, aspect ratio, area, and diameter). In Table 2, the average diameter (µm) and density of the inclusions (parts per mm^2) are given for as-welded and reheated regions. Regarding the inclusion density, there are approximately 1.5 times more inclusions in the as-welded region than in the reheated region. The average size is slightly smaller in the as-welded region with 0.288 µm versus 0.325 µm in the reheated microstructure. Statistically, the most probable inclusion sizes are 0.23 µm in the as-welded and 0.27 µm in the reheated region as shown in Figure 4a. Furthermore, the aspect ratio of all measured inclusions is close to one, indicating that the inclusions are mostly spherical, as expected.

Table 2: Average inclusion size and density in as-welded and reheated microstructure.

Region	Avg. Diam. (µm)	Density (parts per mm^2)
As-welded	0.288	40 805
Reheated	0.325	25 995

The analysis on the potential brittle fracture primary initiators with large size (0.35–5 µm) reveal 9398 inclusions in a total scanned area of 3.69 mm^2, which gives an inclusion density of 2546 (parts per mm^2). The inclusion density with inclusion diameters of the potential brittle fracture primary inclusions is shown in Figure 4b. The smallest and biggest inclusion recorded are of a diameter of 0.32 and 4.69 µm, respectively. However, there are only three inclusions with diameter larger than 1.8 µm in the scanned area. The inclusion density of the potential brittle fracture primary inclusions is very reasonable when comparing to the average results from as-welded and reheated regions in Figure 4a (the accumulated density of particle with diameter above 0.4 µm).

The chemical analyses were made with the electron beam set at 10 keV, which produces an interaction volume with a diameter of about 400 nm on Fe (based on Monte Carlo simulation and comparable to the detected inclusion size). Very limited background signals from the matrix materials were collected, which led to a reasonably precise chemical composition analysis. The average chemical composition of the 9398 large inclusions in weld metal is listed in Table 3.The

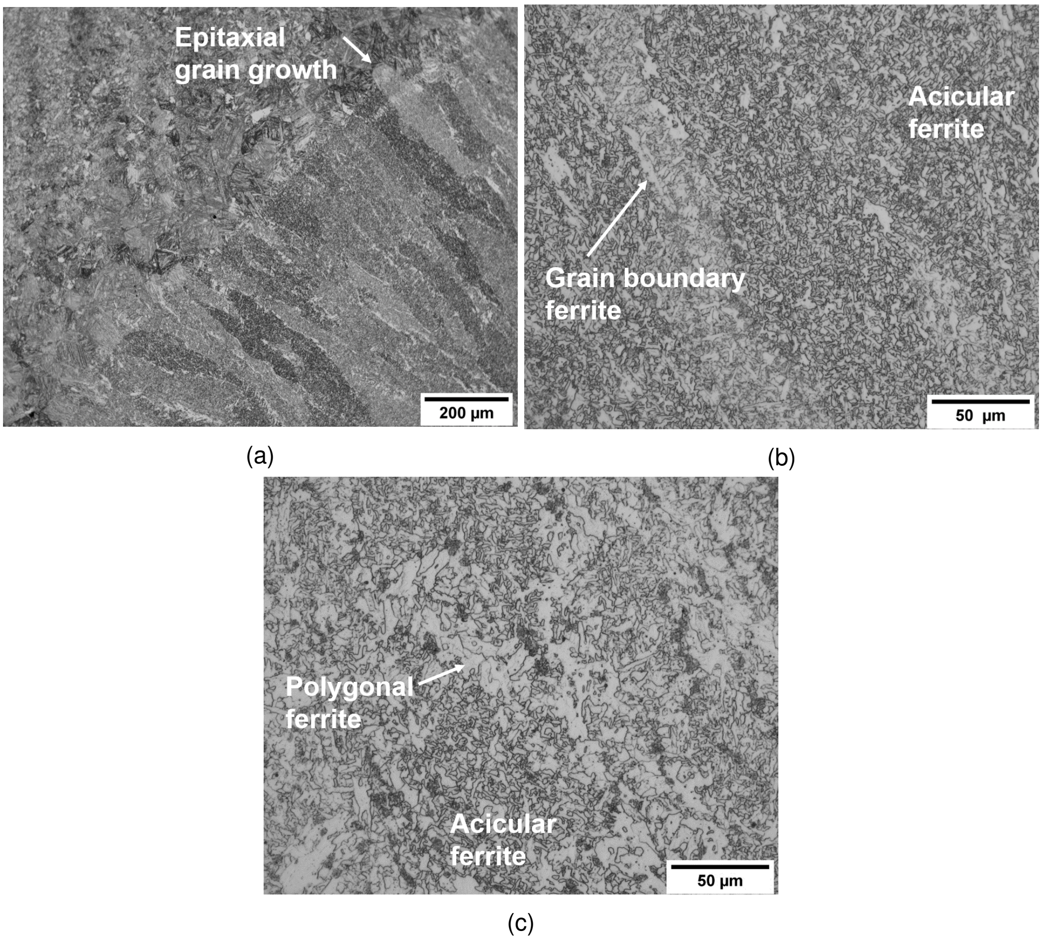

Figure 2: Regions of the weld microstructure. a) Epitaxial growth over the fusion boundary from the parent grain in the CG-HAZ towards the weld solidification bead. b) Weld bead microstructure with acicular ferrite (basket-weave -like structure) and grain boundary ferrite. c) Reheated microstructure containing mainly polygonal ferrite and less acicular ferrite.

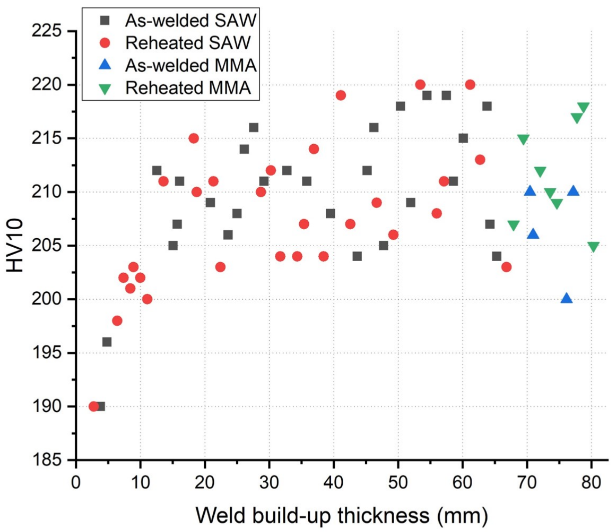

Figure 3: HV10 results through wall thickness. The results are divided into as-welded and reheated regions and SAW and MMA welding methods. The build-up thickness is measured from the inner wall to the outer wall. No significant differences are seen in the macrohardness values between the welding methods or microstructure regions.

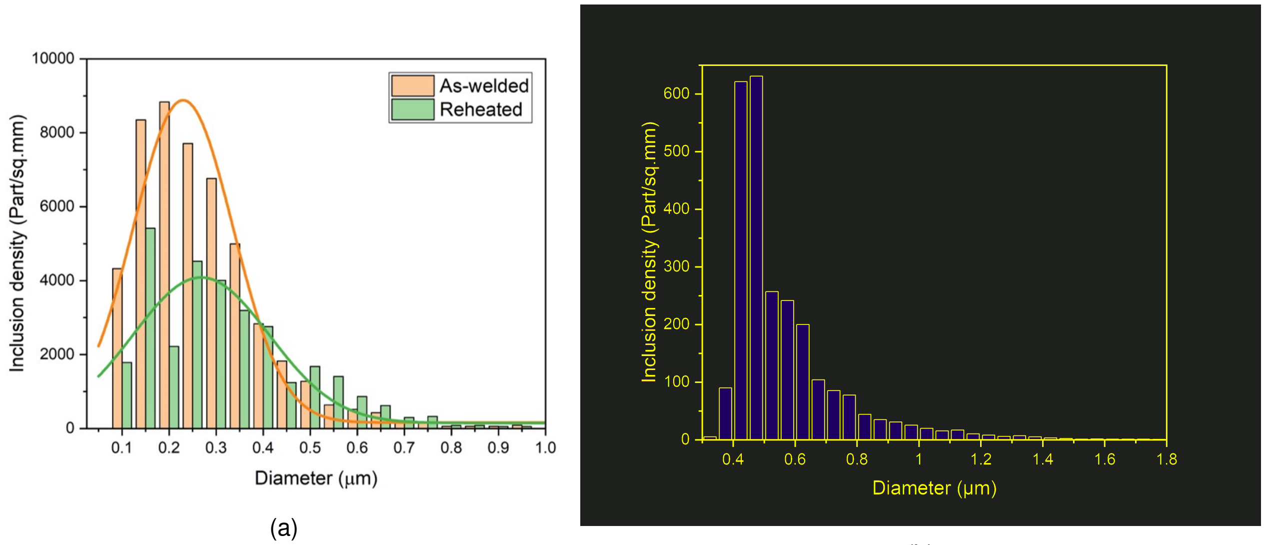

(a)

(b)

Figure 4: a) Inclusion density with inclusion diameters in the as-welded and reheated regions, with the log-normal fitting. b) Inclusion density with inclusion diameters for the potential brittle fracture primary initiator in weld metal. The most statistically probable inclusion sizes are ~0.4–0.5 µm. The smallest and the biggest inclusions recorded are of a diameter of 0.32 and 4.69 µm, respectively.

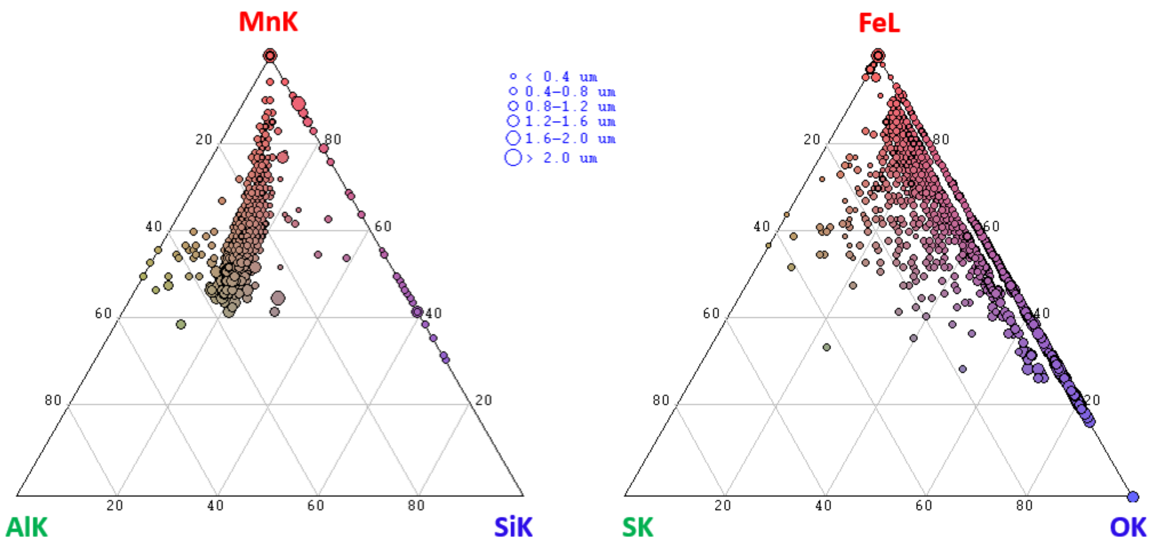

Figure 5: Ternary diagrams of major elements (Mn-Al-Si and Fe-S-O) and size correlations for the potential brittle fracture primary inclusions. The analysis is made with large inclusion particles and the size scale is presented in the middle. The inclusions in the weld metal are mainly Fe-Mn-Al -containing (S)O complex compounds and the mixing oxides contents are much higher than sulphides.

main elements detected are Fe, Mn, Al, Si, O and S. In Figure 5, the main elements are given in ternary diagrams of Mn-Si-Al and S-Fe-O. The element concentration of the inclusion is higher when the circle is closer to the corner and the size of the circle corresponds to the size of the inclusion. The colour of the circle are RGB-mixing in relation to the concentration of the corner colours. The inclusions in the weld metal are mainly Fe-Mn-Al -containing (S)O complex compounds, which consist of mixing oxides (Al-, Si-, Fe-, and Mn-oxide) and sulphides (Mn-, and Fe-sulphide). The size of the inclusions increase with the O and/or Fe concentration. Limited amount of pure oxides or sulphides exist but the amount of pure oxides is at least a magnitude higher than the pure sulphide inclusions.

Table 3: Average chemical composition of potential brittle fracture primary inclusions with larger size (0.35–5 µm) in weld metals.

Element	Fe	Mn	Al	Si	O	S
wt.%	38.02	25.75	11.93	7.26	15.55	1.49

3.3 Fractography

The transition curve in the project was formed by 23 CVN specimens from one-quarter depth of the trepans, in which 9 CVN specimens from the lower shelf were included in the fractographic investigation. Based on the fractography results, the 41 J reference point seems to be where the brittle fracture mechanism changes as the specimens tested above that impact energy did not have a determinable primary fracture site, whereas all the specimens tested at and below 41 J had. Figure 6 shows the full transition curve obtained in the testing. The investigated brittle specimens are from the lower part of the transition curve indicated in the figure.

The reference transition temperatures obtained in the CVN impact toughness testing are $T_{28J} = -85$ ℃, $T_{41J} = -75$ ℃, and $T_{68J} = -60$ ℃, with uncertainty estimated to be ± 5 ℃. These values are similar to those of non-aged reference material, indicating the negligible thermal embrittlement effect. The specimens included in the fractographic investigations are those tested below the transition temperature of $T_{41J} = -75$ ℃ [36].

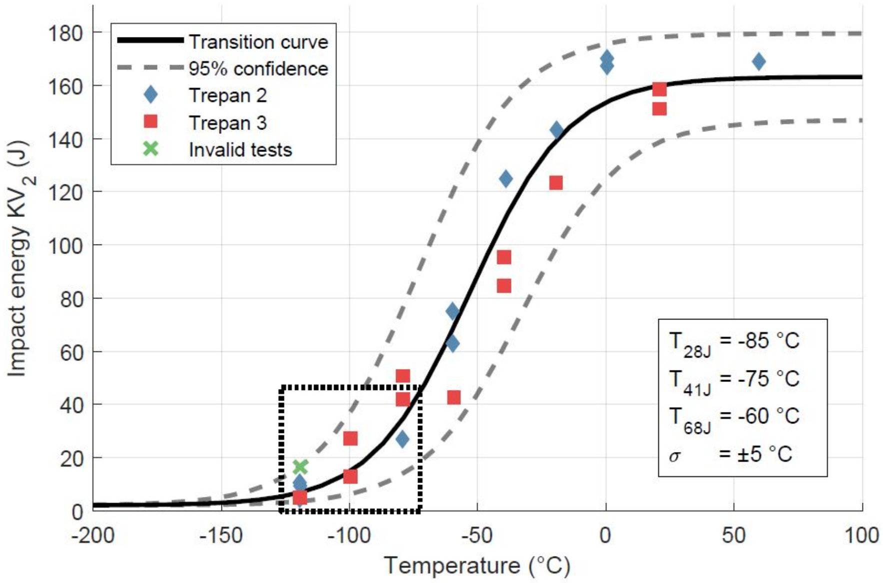

Figure 6: The transition curve of Charpy V-notch impact toughness specimens. The investigated specimens with brittle fracture are inside the square.

In the fracture surface characterisation, the brittle fracture initiated in all specimens by transgranular fracture and an inclusion was found at the primary initiation site in each specimen. An example of brittle fracture surface is seen in Figure 7a, where the initiation site is marked with the red square. The cleavage fracture can be determined according to the characteristic river patterns. In the fractographic examination both mating fracture surfaces were investigated, since the inclusion or part of it may remain on one of the halves. Figure 7b shows the magnified primary initiation site where an inclusion is found. In most of the investigated brittle fracture surfaces, relatively large uncracked inclusions, 1.5–2.5 µm, were detected at the initiation site.

Interdendritic (ID)-like and IG-like fracture areas as the secondary fracture mode in addition to cleavage fracture were found in some of the as-welded and reheated microstructures, respectively. The ID-like fracture surface shown in Figure 8 has presumably propagated along the grain boundary ferrite. This phenomena has also been observed in the reference state, i.e., in the non-aged state of the same material. The fracture is not considered to be brittle, as small dimples and flakes were seen at the ID/IG-like areas. However, the topography imitates the underlying microstructure in these areas. All initiation sites located in the as-welded microstructure, and none in the reheated microstructure. This is evidently due to the location of the notch in the weld bead.

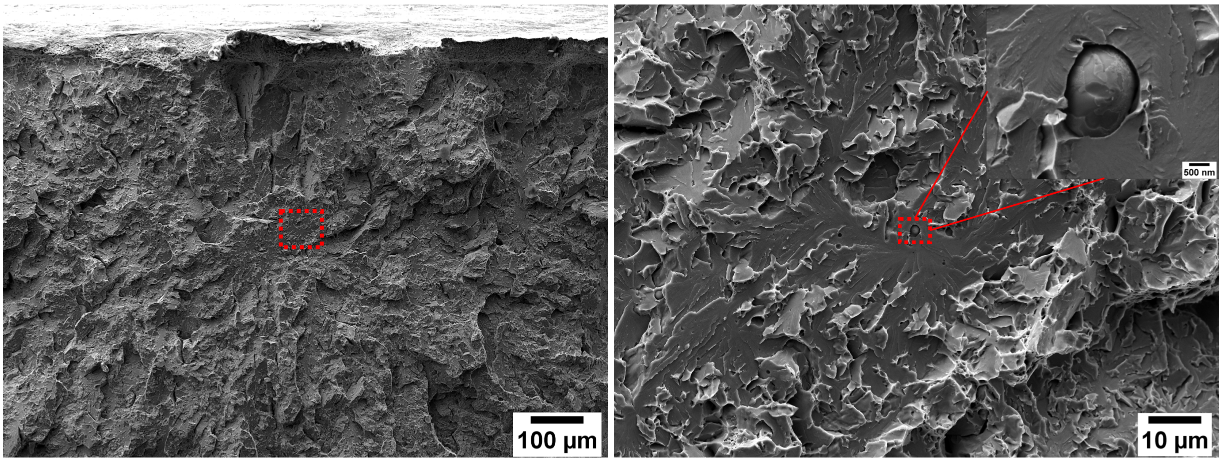

(a) (b)

Figure 7: Brittle cleavage fracture surface and an inclusion at the primary initiation site.

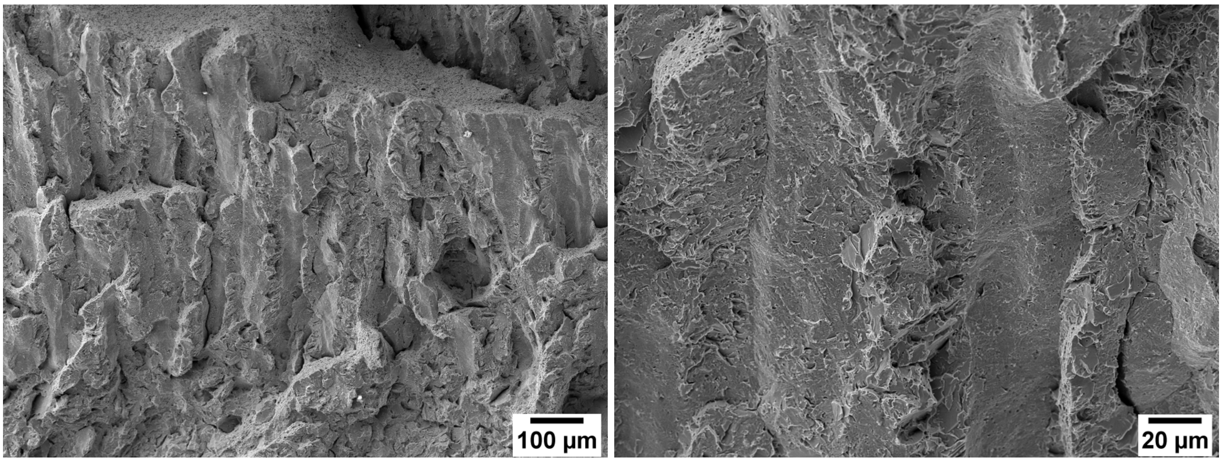

(a) (b)

Figure 8: Interdendritic-like fracture in the as-welded region. The fracture surface is not fully brittle.

4 Discussion

The presence of inclusions has an important effect on the brittle cleavage crack initiation [29]. Weld metals are composed of numerous and rather evenly distributed granular inclusions, different to the base materials, where the inclusions are typically very large and sparsely distributed. The probability of an inclusion with suitable size for brittle fracture initiation is thus much higher in weld metal than in base material, where carbides become the weakest link [18]. The weld bead microstructure contains mainly acicular ferrite and polygonal ferrite, of which acicular ferrite has greater toughness properties. During solidification, the grain boundary ferrite nucleates first at the austenite grain boundaries while the acicular ferrite nucleates at the surface of the non-metallic inclusions [35]. Widmanstätten ferrite may form at the parent austenite grain boundaries in competition with the acicular ferrite. The alloying elements, such as Mn, promote the growth of acicular ferrite over the grain boundary phases [23]. No significant lath structure of Widmanstätten ferrite was observed, which is a result of sufficient alloying and welding parameters. All initiation sites in the investigated specimens with brittle fracture located in the as-welded microstructure. In the reheated region, the larger number of inclusions with bigger size (0.5 – 2.5 µm) is shown in Figure 4a and the larger particles are normally predicted to be the brittle fracture initiators. However, as-welded region with the dendritic microstructure can increase the probability of the brittle fracture initiation, compared to the reheated region with the granular microstructure and shorter crack paths. Further investigations are required to verify the superiority of the influence of the dendritic as-welded microstructure and large multiphase inclusions on brittle fracture initiation.

Correlations between primary initiation particle parameters, size and location, and CVN impact energies less than 41 J, grouped by testing temperature, were plotted in Figure 9. Specimens with larger initiator particles result in relatively lower impact energies when tested at the same temperature as revealed in Figure 9a. The larger particle size (1.5–2.5

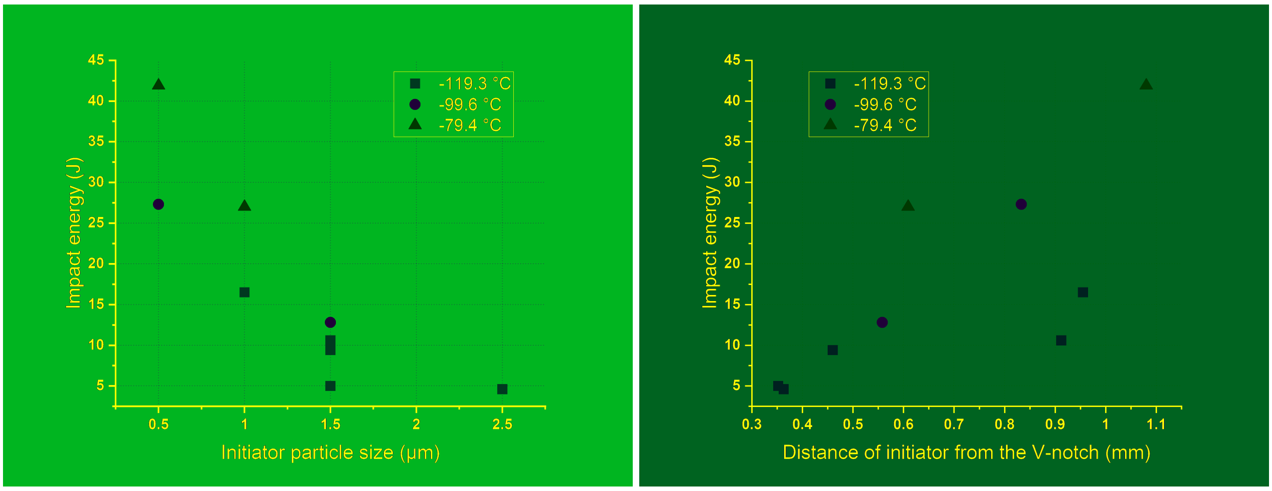

(a) (b)

Figure 9: The relation between primary initiation a) particle size (µm) and b) distance of the initator from the V-notch (mm) with impact energy. The specimens tested in the lower part of the transition curve show a trend, as the weakest location in the process zone of the testing temperature breaks first.

µm) correlates to the impact energy below 15 J. For larger particles the required applied stress to separate the interfaces is lower because the energy release rate increases with the particle size for the same applied stress [28]. The preceding plastic deformation and ductile region before the brittle fracture region in CVN specimens is smaller at low impact energies. Therefore, the primary initiation site is also closer to the V-notch at a lower impact energy as seen in Figure 9b. The inclusion density and size distribution in the studied material show that the brittle fracture tends to initiate from the largest particle in the effective process zone, acting as the weakest locations, and thus, fulfilling the weakest link theory. Nevertheless, a CVN specimen tested at −59.8 °C with impact toughness energy of 62.9 J from the transition region of the DBTT curve has multiple initiation sites, where the primary initiation site is undetectable, in the relative adjacency of the V-notch. Additionally, the initiation particle parameters with impact energy does not fit in the current trend, demonstrating the correlation is only fulfilled with the specimens tested below 41 J in the lower part of the transition curve.

Particle interface debonding is observed in the specimens in the lower part of the transition curve, where the plastic flow is limited. In Figure 7b, a debonded inclusion is shown at a cleavage fracture initiation site. Debonding is normally associated with void nucleation during plastic deformation, when a second-phase particle remains more or less intact. The plastic strain breaks the interatomic bonding between the matrix and the particle instead of breaking the inclusion. The large inclusions increase the local inhomogeneity, which promotes debonding. The interface debonding may initiate a microcrack in the surrounding brittle material and propagate as macroscale cleavage fracture at low temperatures. Depending on the particle size, temperature and chemical composition of the inclusion and the stress state, the microcrack initiates inside the inclusion or at the interface between the inclusion and the weld metal matrix [1, 8, 9, 17, 30, 37, 38]. Hence, multiple active mechanisms are needed to explain the behaviour for aged materials since traditional methodology, i.e., Griffith's theory with failure of an inclusion is not enough without the parallel mechanisms such as debonding of particles and/or grain boundary. In the model developed by Boåsen [20], debonding resulting from thermal ageing was observed when subjected to higher temperatures. The debonding may also be due to segregation of impurities to the particle surfaces, causing reduction of the interface adhesion, since no effect of thermal embrittlement was observed in the impact properties of the investigated weld material. The chemical composition inhomogeneity and weak bonding at the interfaces are the probable causes of debonding to which thermal ageing may have an effect. Additional to the particle debonding, ID- and IG-like failure are observed. These phenomena are related as they result from breaking of the interfaces. While increasing the low-temperature toughness properties, the relatively high Ni content (1.4–2.5 wt%) in the weld metal increases the amount of grain boundary impurity segregation, which then seem to promote the ID/IG-like fracture mode [3, 14]. Moreover, similar, but brittle fracture areas have been detected in specimens with thermal ageing induced embrittlement and the amount of ID/IG fracture was connected with the extent of DBTT shift [3]. The ID/IG fracture area of brittle RPV welds has been related to solute segregation, most commonly phosphorus [21, 25, 39].

According to the semi-quantitative EDS analysis made on the primary initiation sites, the particles at the crack initiation sites are mostly multiphase oxides. The main detected elements were Mn, Si and Al, which are alloying elements in the ferritic weld metal [24]. The multiphase oxide inclusions fulfil the Griffith criterion of brittle fracture initiation. The particle may be brittle due to the intrinsic crystal structure or preceding small defects within the inclusion. Therefore, the inclusion is likely to crack in the presence of plastic strain and further initiate a cleavage fracture. In case of more ductile oxy-sulphides, debonding at the interfaces between uncracked inclusions and weld metal matrix can induce further brittle fracture. Debonding can be concluded to be a result of mild thermal ageing, which is too small to affect the mechanical properties but strong enough to cause debonding rather than particle cracking at the brittle fracture initiation site. However, the effect of thermal ageing below 300 ℃ on debonding caused microcracking still requires further studies.

5 Conclusions

A thermally aged high-Ni low alloyed weld metal from a decommissioned BWR RPV head was investigated. The thermal ageing had, though, not changed the impact toughness of the weld metal. The microstructure characterisation, inclusion analysis and fractographic examination reveal the effects of the microstructure and secondary particles on the brittle fracture initiation. Below are the main findings.

- The as-welded microstructure consists mainly of acicular ferrite. The reheated microstructure consists mainly of polygonal ferrite. Small fractions of grain-boundary ferrite was observed. The amount of grain-boundary ferrite is connected to the observed intergranular- and interdendritic-like fracture surfaces.
- In the as-welded region the inclusion density is approximately 1.5 times higher than in the reheated region. The inclusions are mainly Fe-Mn-Al -containing (S)O complex compounds. All initiation sites in the investigated specimens with brittle fracture located in the as-welded microstructure.
- Brittle fracture primarily initiated from an inclusion with larger size (0.5 – 2.5 µm) in all Charpy V-notch specimens tested from the lower part of the transition curve. The cleavage fracture initiated either within the brittle multiphase oxide inclusions or from the debonded interfaces between the uncracked inclusion and weld metal matrix.
- A trend between the particle size and location with the impact energy was obtained. Lower impact energy is associated with the primary initiation site closer to the V-notch and a larger initiator particle size.
- The primary fracture site can be determined in all specimens tested in the lower part of the transition curve at and below 41 J reference impact toughness energy, but not above, due to the change of the fracture mechanism, and hence the changes in the fracture appearance.

Acknowledgements

Gratefully acknowledging BREDA programme (Barsebäck Research and Development Arena) for providing the research material and SAFIR2022 BRUTE project (Barsebäck RPV material used for true evaluation of embrittlement) for funding the study. The contributions and discussions with M. Boåsen from KTH, S. Lindqvist from VTT and I. Virkkunen from Aalto University are acknowledged.

References

[1] P. Haušild, C. Berdin, and P. Bompard. Prediction of cleavage fracture for a low-alloy steel in the ductile-to-brittle transition temperature range. *Materials Science and Engineering: A*, 391:188–197, 2005. DOI: 10.1016/j.msea.2004.08.067.

[2] A.H. Cottrell. Theory of brittle facture in steel and similar metals. *Trans. Metallurgical Soc. AIME*, 212:192–203, 1958.

[3] P. Joly, L. Sun, P. Efsing, J.P. Massoud, F. Somville, R. Gerard, Y.H. An, and J. Bailey. Characterization of in service thermal ageing effects in base materials and welds of the pressure vessel of a decommissioned PWR pressurizer, after 27 years of operation. 19th Environmental Degradation Conference, 2019.

[4] K. Lindgren, M. Boåsen, K. Stiller, and P. Efsing. Evolution of precipitation in reactor pressure vessel steel welds under neutron irradiation. *Journal of Nuclear Materials*, 488:222–230, 2017.

[5] Yu.A. Nikolaev, A.V. Nikolaeva, A.M. Kryukov, and Yu.N. Korolyov. Radiation embrittlement and thermal annealing behavior of Cr-Ni-Mo reactor pressure vessel materials. *Journal of Nuclear Materials*, 226:144–155, 1995.

[6] G. Odette and R. Nanstad. Predictive reactor pressure vessel steel irradiation embrittlement models: Issues and opportunities. *Journal of The Minerals, Metals & Materials Society*, 61:17–23, 2009.

[7] R. Xing, D. Yu, G. Xie, Z. Yang, X. Wang, and X. Chen. Effect of thermal ageing on mechanical properties of a bainitic forging steels for reactor pressure vessel. *Materials Science and Engineering: A*, 720:169–175, 2018. DOI: 10.1016/j.msea.2018.02.036.

[8] K. Wallin, M. Yamamoto, and U. Ehrnstén. Location of initiation sites in fracture toughness testing specimens - the effect of size and side grooves. In *2016 PVP*, volume 1B. ASME, 2016.

[9] A.A. Griffith. The phenomena of rupture and flow in solids. *Philosophical Transactions of the Royal Society*, A 221:163–197, 1920.

[10] A. Pineau, A.A. Benzerga, and T. Pardoen. Failure of metals I: Brittle and ductile fracture. *Acta Materialia*, 107:424–483, 2016.

[11] W. Weibull. A statistical theory of the strength of materials. *Proc. Roy Swed. Inst. Eng. Res.*, 151:1–53, 1939.

[12] W. Weibull. A statistical distribution function of wide applicability. *Journal of Applied Mechanics*, 18:293–297, 1951.

[13] F. Beremin, A. Pineau, F. Mudry, J.C. Devaux, Y. D'Escatha, and P. Ledermann. A local criterion for cleavage fracture of a nuclear pressure vessel steel. *Metallurgical and Materials Transactions A*, 14:2277–2287, 11 1983.

[14] C. L. Briant and S. K. Banerji. Intergranular failure in steel: the role of grain-boundary composition. *International Metals Reviews*, 23(4):164–199, 1978.

[15] R.W. Hertzberg, R.P. Vinci, and Hertzberg J.L. *Deformation and Fracture Mechanics of Engineering Materials, p.299–311*. 5th edition, 2013.

[16] J. Landes and D. Shaffer. Statistical characterization of fracture in the transition regime. *Fracture Mechanics*, pages 368–382, 1980.

[17] K. Wallin. *Fracture Toughness of Engineering Materials - Estimation and Application*. 2011.

[18] P. Bowen, S.G. Druce, and J.F. Knott. Effects of microstructure on cleavage fracture in pressure vessel steel. *Acta Metallurgica*, 34:1121–1131, 1986.

[19] H. Hein, J. Kobiela, M. Brumovsky, C. Huotilainen, J. Lydman, B. Marini, B. Radiguet, O. Startsev, M. Serrano Garcia, R. Hernandez Pascual, F. Roeder, and H.W. Viehrig. Addressing of specific uncertainties in determination of RPV fracture toughness in the SOTERIA project. Fontevraud 9, 2018.

[20] M. Boåsen. *Modeling of structural integrity of aged low alloy steels using non-local mechanics*. PhD thesis, KTH Royal Institute of Technology, Stockholm, Sweden, 2020.

[21] C.A. Hippsley and S.G. Druce. The influence of phosphorus segregation to particle/matrix interfaces on ductile fracture in a high strength steel. *Acta Metallurgica*, 31:1861–1872, 1983.

[22] H.K.D.H. Bhadeshia and R.W.K. Honeycombe. *Steels: Microstructure and Properties*. Elsevier Ltd, 4th ed. edition, 2017.

[23] G.M. Evans. Effect of manganese on the microstructure and properties of all-weld-metal deposits. *Welding Journal*, pages 64–75, 1980.

[24] J. H. Shim, Y. J. Oh, J. Y. Suh, Y. W. Cho, J. D. Shim, J. S. Byun, and D. N. Lee. Ferrite nucleation potency of non-metallic inclusions in medium carbon steels. *Acta Materialia*, 2001.

[25] B.A. Gurovich, Kulehsova E.A, Y.I. Shtrombakh, O.O. Zabusov, and E.A. Krasikov. Intergranular and intragranular phosphorus segregation in russian pressure vessel steels due to neutron irradiation. *Journal of Nuclear Materials*, 279:259–272, 2000. DOI: 10.1016/S0022-3115(00)00007-6.

[26] D.J. Sprouster, J. Sinsheimer, E. Dooryhee, S.K. Ghose, P. Wells, T. Stan, N. Almirall, G.R. Odette, and L.E. Ecker. Structural characterization of nanoscale intermetallic precipitates in highly neutron irradiated reactor pressure vessel steels. *Scripta Materialia*, 113:18–22, 2016.

[27] K. Lindgren, M. Boåsen, K. Stiller, P. Efsing, and M.) Thuvander. Cluster formation in in-service thermally aged pressurizer welds. *Journal of Nuclear Materials*, 504:23–28, 2018.

[28] J.-S. Byun, J.-H. Shim, Y. W. Cho, and D. N. Lee. Non-metallic inclusion and intragranular nucleation of ferrite in Ti-killed C–Mn steel. *Acta Materialia*, 51(6):1593–1606, 2003.

[29] D.S. Sarma, A.V. Karasev, and P.G. Jönsson. On the role of non-metallic incluisons in the nucleation of acicular ferrite in steels. *ISIJ International*, 49:1063–1074, 2009. DOI: 10.2355/isijinternational.49.1063.

[30] U. Zerbst, R.A. Ainsworth, H.Th. Beier, H. Pisarski, Z.L. Zhang, K. Nikbin, T. Nitschke-Pagel, S. Münstermann, Kucharczyk P., and D. Klingbeil. Review on fracture and crack propagation in weldments - a fracture mechanics perspective. *Engineering Fracture Mechanics*, 132:200–276, 2014.

[31] M. Boåsen, K. Lindgren, J. Rouden, M. Öberg, J. Faleskog, M. Thuvander, and P. Efsing. Thermal ageing of low alloy steel weldments from a Swedish nuclear power plant – a study of mechanical properties. Fontevraud 9, 2018.

[32] M.K. Miller, K.A. Powers, R.K. Nanstad, and P. Efsing. Atom probe tomography characterizations of high nickel, low copper surveillance RPV welds irradiated to high fluences. *Journal of Nuclear Materials*, 437:107–115, 2013.

[33] ISO 148-1:2016 Metallic Materials - Charpy Pendulum Impact Test - Part 1: Test Method. Standard, Finnish Standards Association, 2016.

[34] ASTM E185 -16 Standard Practice for Design of Surveillance Programs for Light-Water Moderated Nuclear Power Reactor Vessels. Standard, ASTM International, 2018.

[35] S.J. Jones and H.K.D.H. Bhadeshia. Competitive formation of inter- and intragranularly nucleated ferrite. *Metallurgical and Materials Transactions A*, 28A:2005–2013, 1997.

[36] N. Hytönen. Effect of microstructure on brittle fracture initiation in a reactor pressure vessel weld metal, 2019. Master of Science Thesis.

[37] T. Anderson. *Fracture Mechanics Fundamentals and Applications*. CRC Press, Inc., 2nd ed. edition, 1995.

[38] M. Kroon and J. Faleskog. Micromechanics of cleavage fracture initiation in ferritic steels by carbide cracking. *Journal of the Mechanics and Physics of Solids*, 53:171–196, 2005.

[39] L. Zhang, B. Radiguet, P. Todeschini, C. Domain, Y. Shen, and P. Pareige. Investigation of solute segregation behavior using a correlative EBSD/TKD/APT methodology in a 16MND5 weld. *Journal of Nuclear Materials*, 523:434–443, 2019.